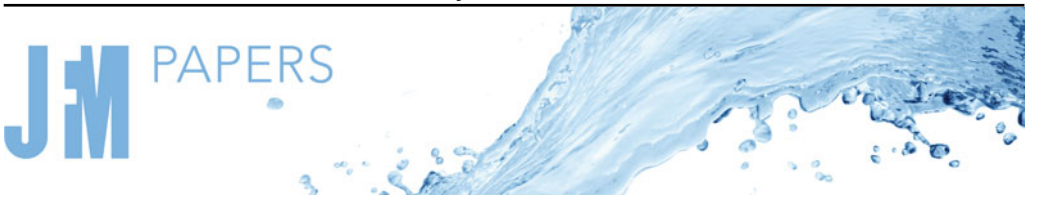
J. Fluid Mech. (2026), *vol.* 1045, A3, doi:10.1017/jfm.2026.12110



An analytical model for rotors in confined flow across operating regimes

Ilan M.L. Upfal[1], **Kiley J. McClure**[1], **Kirby S. Heck**[1], **Supun Pieris**[2], **John W. Kurelek**[2], **Marcus Hultmark**[3] and **Michael F. Howland**[1]

[1]Civil and Environmental Engineering, Massachusetts Institute of Technology, Cambridge, MA 02139, USA

[2]Mechanical and Materials Engineering, Queen's University, Kingston, Ontario K7L 3N6, Canada

[3]Mechanical and Aerospace Engineering, Princeton University, Princeton, NJ 08544, USA

Corresponding author: Michael F. Howland, mhowland@mit.edu

(Received 6 March 2026 UTC; revised 13 August 2026 UTC; accepted 19 August 2026 UTC)

Rotors operating in confined flows, or blockage, are commonly encountered in wind and water tunnels, as well as in shallow or dense deployments of hydrokinetic turbines. Confinement induces a streamwise pressure gradient in the channel, modifying the rotor induction, thrust and power. To account for these effects, physics-based or empirical blockage corrections are used as a transfer function between the dynamics of an object operating in confined and unconfined settings. However, existing blockage models are largely only applicable to rotors operating at relatively low thrust coefficients, such that the assumptions of classical momentum theory are valid. Further, rotors are often partially misaligned with the inflow, which modifies both the geometric blockage and the thrust force, whereas existing blockage models assume perfectly aligned flow conditions. We develop a generalised engineering model for an actuator disk operating in confined flow at arbitrary misalignment angles and thrust coefficients, termed the Unified Blockage Model (UBM). The analytical model shows excellent agreement with large eddy simulations of an actuator disk and elucidates the coupled interactions between thrust, misalignment and blockage. To predict bladed rotor dynamics, the UBM is incorporated into a blade-element momentum model framework and validated against blade-resolved simulations across a wide range of tip-speed and blockage ratios. Finally, a blockage correction method is developed based on the UBM and validated against a suite of numerical and experimental data.

Key words: aerodynamics, wakes

© The Author(s), 2026. Published by Cambridge University Press. This is an Open Access article, distributed under the terms of the Creative Commons Attribution licence (https://creativecommons.org/licenses/by/4.0/), which permits unrestricted re-use, distribution and reproduction, provided the original article is properly cited.

https://doi.org/10.1017/jfm.2026.12110 Published online by Cambridge University Press

1. Introduction

Fast-running predictive models for the performance of turbomachines, including hydrokinetic/wind turbines and propellers, largely rely on momentum theory (Rankine 1865; Froude 1878; Froude 1889). Turbomachine rotors generate thrust forces that are either opposing (turbines) or in the direction of the flow (propellers). Given this thrust force, the velocity at the rotor cross-section differs from the free-stream velocity by the velocity induced by the thrust (induction) which is a consequence of the pressure difference (Sørensen 2016). To predict the induced velocity, momentum theory represents the rotor as a porous actuator disk that imparts a uniform thrust force on the surrounding flow. Originally derived for propellers, momentum theory is now widely used in the design and analysis of hydrokinetic and wind turbines (Sørensen 2011; Adcock *et al.* 2021). Simple optimisation of the operating conditions (thrust coefficient) using the momentum theory model results in the well-known Lanchester–Betz–Joukowsky limit (Van Kuik 2007), which predicts the theoretical maximum efficiency (coefficient of power) for a turbine operating in unconfined flow. To yield a fully predictive model of rotor thrust, power and wake dynamics, the induction predictions from momentum theory can be coupled with a blade-element model (Glauert 1935) that predicts the thrust coefficient based on lift and drag forces on rotating hydro/aerofoils. The lift and drag forces depend on the velocity at the rotor (induction), yielding the blade-element momentum (BEM) approach (e.g. Vogel *et al.* 2018; Madsen *et al.* 2020). Therefore, accurate BEM predictions rely on both a blade-element model that predicts blade-level forces given a known velocity field at the rotor, as well as a momentum closure that predicts the velocity field at the rotor considering the geometry and dynamics of the flow. However, in many engineering applications, turbomachines operate in flow configurations that are not appropriately described by classical momentum theory due to its simplifying assumptions, geometric arguments and boundary conditions.

Hydrokinetic turbines used in tidal and river energy harvesting often operate in confined settings where blockage, the ratio between the swept area of the turbine and the channel cross-section, is not negligible (Garrett & Cummins 2005). Similarly, in experimental wind tunnels (Barlow *et al.* 1999) and water flumes (Ross & Polagye 2020), blockage can significantly affect the dynamics and performance of turbomachines (Chen & Liou 2011). Although the swept area of wind turbines is often much smaller than the cross-section of the atmospheric boundary layer, shallow boundary layer heights and large, dense wind farms can also trigger significant blockage effects and associated pressure gradients (Ndindayino *et al.* 2025).

Meanwhile, turbomachines often operate in non-ideal settings where the mean inflow is not aligned with the rotor. Such circumstances are common for hydrokinetic/wind turbines because of the chaotic, turbulent environmental flow in which they operate, along with slowly reacting yaw controllers (Fleming *et al.* 2014; Frost *et al.* 2015, 2017; Piano *et al.* 2017). Recent attention has also focused on wake steering, where the wake is laterally deflected by intentional yaw misalignment, to increase the performance of turbine arrays (Fleming *et al.* 2019; Howland *et al.* 2022; Meyers *et al.* 2022). Similarly, propellers frequently operate in misalignment, often called drift (Di Mascio *et al.* 2014).

Classical momentum theory does not account for the confined and misaligned settings described above, which can yield significant error in predictive models. The first-order effects of blockage and inflow-rotor misalignment are to generate pressure gradients and lateral velocities, respectively, which are not modelled in classical momentum theory. Substantial previous effort has been made to model the effect of blockage on rotor dynamics, starting with Glauert (1935), which is based on a linearisation in the

https://doi.org/10.1017/jfm.2026.12110 Published online by Cambridge University Press

low-blockage regime. More recent studies (Mikkelsen & Sørensen 2002; Bahaj *et al.* 2007; Garrett & Cummins 2007; Werle 2010; Segalini & Inghels 2014; Vogel *et al.* 2018; Ndindayino *et al.* 2025) have developed improved models for the effects of flow confinement on rotor dynamics. A further limitation of existing blockage models and blockage corrections that are extensions of classical momentum theory is that they cannot predict the dynamics of high-thrust rotors (Ross & Polagye 2020), because momentum theory is not applicable for high-thrust rotors due to the assumption that the wake pressure recovers back to the free-stream pressure (Roshko 1955). This limitation has been recently addressed in unconfined flows (Steiros & Hultmark 2018; Liew *et al.* 2024). Building on the model proposed in Steiros & Hultmark (2018), Steiros *et al.* (2022) proposed a closed-form, analytical extension to simultaneously account for high-thrust rotors and confined flow, but it assumes perfect alignment between the rotor and the inflow. Separately, recent efforts have focused on modelling rotors operating in misalignment with the inflow (Bastankhah & Porté-Agel 2016; Shapiro *et al.* 2018; Heck *et al.* 2023; Tamaro *et al.* 2024). In parallel, Liew *et al.* (2024) developed an extension of classical momentum theory for unconfined flow that yields low error across the thrust coefficients and rotor-inflow misalignment angles relevant to wind turbines, but it does not capture confinement effects. To summarise, there is a need for a generalised momentum model which can address blockage, rotor-inflow misalignment and arbitrary thrust coefficients of realistic rotors in a unified framework for applications including BEM engineering modelling and blockage corrections. Such a model should both accurately predict key quantities at the rotor, such as the induction, thrust and power, and should also accurately predict the wake and bypass velocities and pressure that are consistent with conservation of mass, momentum and energy.

In this study, we extend the work of Liew *et al.* (2024) to develop a generalised momentum theory that accounts for blockage, rotor-inflow misalignment and arbitrary thrust coefficients. The analytical model, hereafter referred to as the Unified Blockage Model (UBM), is validated against large eddy simulations (LES) of an actuator disk across 80 independent combinations of blockage ratios, thrust coefficients and misalignment angles. We further incorporate the UBM within a BEM framework to predict the performance of bladed rotors under arbitrary blockage and misalignment, and validate the results against blade-resolved simulations. Finally, we present a new blockage correction method, which is a widely used approach for mapping rotor measurements between blockage ratios, based on the UBM. The blockage correction method is evaluated in comparison with computational fluid dynamics (CFD) simulations as well as experiments of an axial flow hydrokinetic turbine.

The remainder of this paper is organised as follows. The UBM, a generalised momentum model for confined rotors, is derived and integrated into BEM and blockage correction methods in § 2. The LES methodology used to validate the UBM is described in § 3. We present the results of the model predictions in § 4. Finally, the key findings of the work are summarised in § 5.

2. A generalised framework for modelling confined rotors

In this section, we derive the UBM in § 2.1, which is a generalisation of the Unified Momentum Model (UMM) (Liew *et al.* 2024) to confined flow. Next, in § 2.2, the UBM is coupled with a blade-element closure yielding a fully predictive model for bladed rotors, termed the Unified BEM model. Finally, a method for applying the UBM to account for blockage in measurements of rotor thrust and power (a blockage correction) is developed in § 2.3.

https://doi.org/10.1017/jfm.2026.12110 Published online by Cambridge University Press

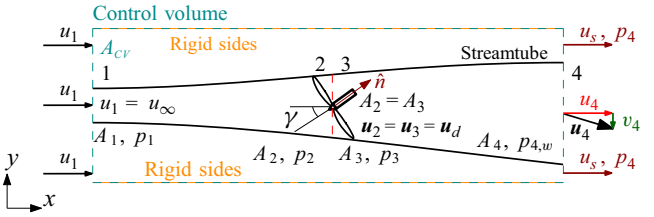


Figure 1. Control volume for analysis of a confined, misaligned turbine. The streamwise and spanwise directions are x and y, respectively. The turbine is yaw/tilt misaligned at angle γ, where positive misalignment is a counter-clockwise rotation. The sides of the control volume are rigid so there is no mass flux through them. As in classical momentum theory, we consider four stations for the analysis, and the flow variables are labelled with the corresponding station as subscript numbers. The cross-sectional areas, streamwise velocities, spanwise velocities and pressures are denoted as A, u, v and p, respectively. The pressure at the outlet is $p_{4,w}$ within the streamtube and p_4 outside of the streamtube. The unit vector normal to the misaligned turbine is $\hat{n}$.

2.1. *A blockage model for misaligned actuator disks across thrust coefficients*

We aim to develop an analytical model for the induction, thrust and power of an actuator disk accounting for flow confinement (blockage), misalignment between the inflow and rotor, and arbitrary thrust coefficients, including high-thrust operation. The non-dimensional parameter describing the rotor-normal, rotor-averaged induced velocity is (Heck *et al.* 2023)

$$a_n = 1 - \frac{\boldsymbol{u}_d \cdot \hat{n}}{u_\infty \cos(\gamma)}, \tag{2.1}$$

which is the generalisation of the standard (axial) induction factor in classical one-dimensional momentum modelling (Van Kuik 2007). The rotor-averaged velocity at the rotor disk is $\boldsymbol{u}_d$, the free-stream velocity is u_∞, and the misalignment angle between the inflow and the rotor-normal vector $\hat{n}$ is γ. As a result of misalignment, the rotor-induced velocity will vary azimuthally (Glauert *et al.* 1926). Following Heck *et al.* (2023), the present analytical model is derived in terms of the rotor-averaged induction factor. Therefore, the model predictions will not depend on the azimuthal variations. To derive a model for the induction factor a_n, it is convenient to describe the rotor aerodynamics (i.e. blade aerofoil properties, number of blades, etc.) and control (tip-speed ratio, blade pitch angle, etc.) with a single parameter, the local thrust coefficient C_T'. The thrust force for the actuator disk is thus defined as (Calaf *et al.* 2010)

$$\boldsymbol{F}_T = -\frac{1}{2}\rho C_T' A_d (\boldsymbol{u}_d \cdot \hat{n})^2 \hat{n}, \tag{2.2}$$

where ρ is the fluid density and $A_d = \pi D^2/4$ is the rotor area, with D the rotor diameter. We will explicitly connect the value of C_T' to the rotor design and control properties in § 2.2.

We now consider analysis of the control volume shown in figure 1, which has rigid sides that are slip walls. This is appropriate for wind (Mikkelsen & Sørensen 2002) and water (Ross & Polagye 2020) tunnels and also for hydrokinetic turbine settings in low Froude number regimes (Garrett & Cummins 2007). Following standard momentum theory, we consider turbulence-free, uniform inflow. We include the effects of the confining channel walls through a no-penetration condition only (i.e. slip walls); wall boundary layer effects such as shear and turbulence are not included. The flow is assumed to be inviscid (frictionless) within the control volume. Therefore, the model is applicable to the rotor and near wake in which turbulent mixing does not yet contribute to the dynamics (Burton *et al.*

https://doi.org/10.1017/jfm.2026.12110 Published online by Cambridge University Press

2011; Bastankhah & Porté-Agel 2016). The exit of the control volume at station 4 is taken to be the location at which the shear layers around the potential core meet causing the wake to become fully turbulent, known as the near-wake length (Lee & Chu 2003; Bastankhah & Porté-Agel 2016). The present model assumes uniform blockage and does not capture potential impacts of channel asymmetry on the rotor dynamics, relevant for applications such as tidal turbines in close proximity to walls/surfaces. For example, wall proximity could influence lateral induced velocities resulting from rotor-inflow misalignment. The free-stream velocity and pressure are denoted u_∞ and p_1, respectively. The velocity and pressure at the outlet outside of the streamtube are u_s and p_4, respectively. To allow for the additional pressure deficit within the wake associated with base-suction effects at high thrust (Liew *et al.* 2024), the outlet pressure inside the streamtube is defined as $p_{4,w}$. The streamwise and lateral wake velocities at the streamtube outlet are u_4 and v_4, respectively. Conservation of streamwise momentum in the control volume yields

$$\boldsymbol{F}_T \cdot \hat{i} = \rho u_4^2 A_4 + \rho u_s^2 (A_{CV} - A_4) - \rho u_\infty^2 A_{CV} + A_{CV}(p_4 - p_1) + A_4(p_{4,w} - p_4), \tag{2.3}$$

where A_4 is the area of the streamtube at station 4, and A_{CV} is the cross-sectional area of the control volume in the yz-plane. Conservation of energy inside the streamtube implied by the Bernoulli equation yields (Liew *et al.* 2024)

$$a_n = 1 - \sqrt{\frac{u_\infty^2 - u_4^2 - v_4^2}{C_T' \cos^2(\gamma) u_\infty^2} - \frac{(p_{4,w} - p_1)}{\frac{1}{2}\rho C_T' \cos^2(\gamma) u_\infty^2}}. \tag{2.4}$$

The Bernoulli equation applied along a streamline outside the streamtube that is inside that control volume is

$$\frac{1}{2}\rho u_\infty^2 + p_1 = \frac{1}{2}\rho u_s^2 + p_4, \tag{2.5}$$

where u_s is the bypass velocity that can be larger than u_1 due to the flow confinement. This application of the Bernoulli equation neglects any potential turbulent mixing between the wake and bypass flow (Nishino & Willden 2012, 2013), which is found to be negligible in the near wake within the present LES cases with zero free-stream turbulence inflow. Mass conservation in the streamtube between the actuator disk and outlet gives

$$u_\infty (1 - a_n) \cos(\gamma) A_d = u_4 A_4, \tag{2.6}$$

and mass conservation in the control volume gives

$$A_{CV}\, u_\infty = u_4 A_4 + (A_{CV} - A_4) u_s. \tag{2.7}$$

The mass flux out of the control volume at the rigid sides is explicitly zero in this equation. Finally, the lateral velocity generated by misalignment is modelled based on Prandtl lifting line theory which yields an analytical solution for the constant transverse velocity induced by an elliptical lift distribution (Shapiro *et al.* 2018; Heck *et al.* 2023)

$$v_4 = -\frac{1}{4} C_T' (1 - a_n)^2 \sin(\gamma) \cos^2(\gamma) u_\infty. \tag{2.8}$$

This formulation was shown to accurately predict the lateral induced velocity of an unconfined actuator disk across a range of misalignment and thrust coefficients. However, the expression slightly overpredicted the lateral induced velocity for higher thrust values ($C_T' \sim 10$) (Liew *et al.* 2024).

https://doi.org/10.1017/jfm.2026.12110 Published online by Cambridge University Press

Combining (2.3)–(2.8) yields a system of six coupled nonlinear equations which is the final form of the UBM

$$a_n = 1 - \sqrt{\frac{u_\infty^2 - u_4^2 - v_4^2}{C_T' \cos^2(\gamma) u_\infty^2} + \frac{(p_1 - p_{4,w})}{\frac{1}{2}\rho C_T' \cos^2(\gamma) u_\infty^2}}, \tag{2.9}$$

$$\frac{u_4}{u_\infty} = \frac{A_d}{A_4}(1 - a_n)\cos(\gamma), \tag{2.10}$$

$$\frac{v_4}{u_\infty} = -\frac{1}{4}C_T'(1 - a_n)^2 \sin(\gamma)\cos^2(\gamma), \tag{2.11}$$

$$\frac{u_s}{u_\infty} = 1 + \frac{\beta A_4(u_\infty - u_4)}{(A_d - \beta A_4)u_\infty}, \tag{2.12}$$

$$\frac{A_4}{A_d} = \frac{\frac{1}{2}C_T'(1 - a_n)^2 \cos^3(\gamma)u_\infty^2 + (1/\beta)(u_s^2 - u_\infty^2 - (p_1 - p_4)/\rho)}{(p_4 - p_{4,w})/\rho + u_s^2 - u_4^2}, \tag{2.13}$$

$$\frac{p_1 - p_4}{\rho u_\infty^2} = \frac{1}{2}(u_s^2/u_\infty^2 - 1), \tag{2.14}$$

where $\beta = A_d/A_{CV}$ is the geometric blockage ratio. The UBM comprises six equations, but contains seven unknowns. The wake pressure $p_{4,w}$ is the unclosed term. Liew *et al.* (2024) developed a model for the base suction of a turbine operating in unconfined flow. This is a region of persistent pressure deficit directly downstream of a highly loaded rotor, resulting from its high induction factor. The UMM predicts this base-suction pressure deficit using a rapid solution to the pressure Poisson equation associated with the two-dimensional inviscid Euler equations. In the following discussion, we describe the extension of the UMM pressure prediction to account for blockage.

Based on our suite of LES in this study, we observe that the wake pressure becomes homogeneous across the entire outlet ($p_{4,w} = p_4$) in the limit of high blockage. Specifically, the pressure difference between the wake and bypass flows becomes negligible compared with the much larger pressure gradient resulting from blockage. On the other hand, the near-wake wake pressure $p_{4,w}$ significantly departs from the outer pressure p_4 for low blockage and high thrust, as captured by the UMM (Liew *et al.* 2024). When the blockage ratio is very small and the free-stream inflow has no turbulence, the turbulent mixing does not significantly contribute to the dynamics within the wake potential core until the near-wake length (Liew *et al.* 2024; Heck *et al.* 2026). In our zero free-stream turbulence LES of an actuator disk in confined flow, the role of turbulence entrainment in the near wake also has a small effect on the rotor dynamics, both within the potential core and in the bypass flow, compared with the large impact of the bypass flow pressure. Other studies have proposed turbulence entrainment from the bypass flow into the near wake as a mechanism for increasing the rotor power extraction (Nishino & Willden 2012, 2013; Dehtyriov 2023). For example, using Reynolds-averaged Navier Stokes simulations of an actuator disk in confined flow, Nishino & Willden (2012) found that near-wake entrainment increased rotor power and thrust when blade-induced or free-stream turbulence was added to the simulation, relative to a turbulence-free inflow baseline. Studying the near-wake turbulent transport across inflow conditions and rotor representations should be explored in future work. The UMM (Liew *et al.* 2024) wake

https://doi.org/10.1017/jfm.2026.12110 Published online by Cambridge University Press

pressure solution is an inviscid solution based on unconfined flow that does not account for any potential effects from confinement, including possible turbulent shear stress at higherblockage ratios (Nishino & Willden 2012, 2013), free-stream turbulence (Nishino & Willden 2012; Dehtyriov 2023) or possible inviscid effects associated with confinement on the solution of the pressure Poisson equation. As such, we model the pressure difference between wake and bypass flows as $p_{4,w} - p_4 = (1-\beta)p_{UMM}(C_T', \gamma)$, where p_{UMM} is the pressure deficit given by the UMM (Liew *et al.* 2024) for unconfined flows. This hybrid pressure model captures the departure of the wake pressure from the outer pressure in the low-blockage regimes ($\beta \to 0$) and captures the convergence of the wake and outer pressure for higher-blockage values. For completeness, a description of the UMM pressure closure is included in Appendix A and a sensitivity analysis to the hybrid pressure closure is presented in Appendix B. This formulation yields high accuracy across β and C_T' by yielding the correct limiting behaviour for high thrust and low blockage, and returning to a constant wake pressure for high blockage. Section 4.1 provides validation of the pressure closure against LES. Future work may consider extending the UBM to account for potential impacts of turbulent mixing between the wake and the bypass flow (Nishino & Willden 2013) on the wake pressure difference ($p_{4,w} - p_4$) measured at station 4 (where the shear layers around the potential core meet) in confined conditions. In the present LES data with zero free-stream turbulence inflow, the pressure difference between the wake and bypass flow at station 4 ($p_{4,w} - p_4$) is negligible relative to the pressure difference induced by confinement ($p_1 - p_4$) for all blockage ratios except for approximately unblocked conditions ($\beta = 0.005$).

As described previously, the local thrust coefficient C_T' is a useful input quantity since it compactly represents the rotor design and control settings. Further, C_T' is independent of the misalignment angle γ and the blockage ratio β. Often, rotors are characterised by a thrust coefficient C_T, which is defined as $C_T = 2\|\boldsymbol{F}_T\|/(\rho A_d u_\infty^2)$, where $\|\boldsymbol{F}_T\|$ is the magnitude of the thrust force. Equations (2.9)–(2.14) describing the UBM can be closed when C_T is used as the input thrust coefficient variable instead of C_T' by adding an additional equation to the set above

$$C_T' = \frac{C_T}{(1-a_n)^2\cos^2(\gamma)}. \tag{2.15}$$

Note that the thrust coefficient C_T depends on the local thrust coefficient C_T', the misalignment angle γ and the blockage ratio β (the effect of the blockage ratio comes through the induction factor a_n).

To summarise, the model solved using C_T' as the input thrust variable and (2.9)–(2.14) can be written compactly as

$$[a_n,\ u_4/u_\infty,\ v_4/u_\infty,\ u_s/u_\infty,\ A_4/A_d,\ (p_1-p_4)/\rho u_\infty^2] = f_{Unified}(C_T', \gamma, \beta) \tag{2.16}$$

and will be referred to as the C_T'-formulation. When using C_T as the input thrust variable together with (2.9)–(2.15), the model can be written as

$$[a_n,\ u_4/u_\infty,\ v_4/u_\infty,\ u_s/u_\infty,\ A_4/A_d,\ (p_1-p_4)/\rho u_\infty^2,\ C_T'] = f_{Unified}(C_T, \gamma, \beta) \tag{2.17}$$

and will be referred to as the C_T-formulation. Here, $f_{Unified}$ denotes the converged solution to the appropriate set of equations.

The nonlinear coupled system is solved using a standard root-finding algorithm. As with most such methods, fast and reliable convergence depends on providing a suitable

https://doi.org/10.1017/jfm.2026.12110 Published online by Cambridge University Press

initial guess. When solved with the C_T'-formulation, initial guesses for induction a_n and wake velocities u_4/u_∞ and v_4/u_∞ are obtained directly from the UMM (Liew *et al.* 2024) which is the limit of $\beta \to 0$. These are combined with $A_4/A_d = (1-a_n)\cos(\gamma)(u_\infty/u_4)$, together with Eqs. 2.12 and 2.14 to determine u_s/u_∞ and $(p_1-p_4)/\rho u_\infty^2$. Since the initial guess is given by the $\beta \to 0$ limit, this initial guess can be too far from the final solution for large values of β. So for larger values of β (e.g. $\beta = 0.3$), we first solve the model for $\beta = 0.1$ based on initialisation from the $\beta = 0$ limiting case as described above, then we solve the model at $\beta = 0.2$ with initialisation from the $\beta = 0.1$ results and so on until the solution at the desired β is reached. When solved using the C_T-formulation, initial guesses are generated via pre-tabulation. First, the C_T'-formulation is solved across a range of C_T', γ and β which gives the corresponding values of C_T using (2.15). Then, the desired initial guesses for the model outputs $(a_n,\ u_4/u_\infty,\ v_4/u_\infty,\ u_s/u_\infty,\ A_4/A_d,\ (p_1-p_4)/\rho u_\infty^2,\ C_T')$ are tabulated as a function of the input variables (C_T, γ, β). Initial guesses for any combination of input variables can then be obtained using linear interpolation. A reference implementation of the UBM is available as an open-source Python library (https://doi.org/10.5281/zenodo.20644355) (Liew *et al.* 2026*b*).

In the limit of zero misalignment and low thrust coefficients, the UBM returns to the actuator disk model developed by Garrett & Cummins (2007) for confined flow, while in the limit of zero blockage ($\beta \to 0$), the model yields the UMM for unconfined flows developed by Liew *et al.* (2024). As will be shown in § 4.1, nonlinear interactions arise between blockage, thrust coefficient and misalignment angle, such that the previous models cannot be superposed and instead must be modelled jointly, as the present approach provides.

2.2. *A generalised blade-element momentum model for rotors in confinement*

The UBM presented in the previous section predicts the induced velocities, and therefore the velocity at the rotor, based on an input blockage ratio, misalignment angle and thrust coefficient. However, the thrust coefficient for an arbitrary rotor design and control strategy is not known *a priori*. Here, a blade-element model is used to calculate the thrust coefficient based on the velocity at the rotor, the aerofoil properties, misalignment angle, blade pitch angle and tip-speed ratio. The blade-element model is solved on a polar grid depending on radial and azimuthal position (μ, ψ). These positions are formulated non-dimensionally, with non-dimensional radius $\mu = r/R$, where $R = D/2$ is the rotor radius and r is the radial coordinate, and ψ in radians. The tip-speed ratio is $\lambda = R\Omega/u_\infty$, where Ω is the angular velocity of the rotor. The axial and tangential velocity components relative to the blades are

$$v_n(\mu, \psi) = (1-a_n)\cos(\gamma)u_\infty, \tag{2.18}$$

$$v_t(\mu, \psi) = (1+a')\lambda\mu u_\infty - (1-a_n)\cos(\psi)\sin(\gamma)u_\infty, \tag{2.19}$$

assuming uniform inflow, where a' is the tangential induction factor. The speed w and angle ϕ of the flow relative to the blades are

$$w^2(\mu, \psi) = v_n^2(\mu, \psi) + v_t^2(\mu, \psi), \tag{2.20}$$

$$\phi(\mu, \psi) = \tan^{-1}\left(\frac{v_n(\mu, \psi)}{v_t(\mu, \psi)}\right). \tag{2.21}$$

The lift and drag coefficients, C_l and C_d, are evaluated as a function of the local angle of attack $\alpha(\mu, \psi) = \phi(\mu, \psi) - \theta_t(\mu) - \theta_p$, where θ_t and θ_p are the blade twist and pitch

https://doi.org/10.1017/jfm.2026.12110 Published online by Cambridge University Press

angles respectively. Transforming into the rotor frame, the rotor-normal and tangential force coefficients are

$$C_n(\mu, \psi) = \cos(\phi) C_l(\mu, \alpha(\mu, \psi)) + \sin(\phi) C_d(\mu, \alpha(\mu, \psi)), \tag{2.22}$$

$$C_{tan}(\mu, \psi) = \sin(\phi) C_l(\mu, \alpha(\mu, \psi)) - \cos(\phi) C_d(\mu, \alpha(\mu, \psi)). \tag{2.23}$$

Finally, the thrust coefficient is

$$C_T(\mu, \psi) = \sigma(\mu) C_n(\mu, \psi) \frac{w^2(\mu, \psi)}{u_\infty^2}, \tag{2.24}$$

with blade solidity $\sigma(\mu) = Bc/2\pi r$, where B is the number of blades and $c(\mu)$ is the blade chord. To account for reductions in the blade force coefficients due to the effects of tip vortices, we apply a standard tip loss correction factor

$$F(\mu) = \frac{2}{\pi} \arccos\left[\exp\left(-\frac{B(1-\mu)}{2\mu \sin\phi}\right)\right], \tag{2.25}$$

and use a modified axial force as input to the induction model (Madsen *et al.* 2020)

$$C_T^{corr}(\mu, \psi) = \frac{C_T(\mu, \psi)}{F(\mu)}. \tag{2.26}$$

The rotor-normal and tangential induction factors are initialised with $a_n(\mu, \psi) = 1/3$ and $a'(\mu, \psi) = 0$, respectively. At each iteration, equations (2.18)–(2.26) are solved to update the rotor normal and tangential forces based on the current values of $a_n(\mu, \psi)$ and $a'(\mu, \psi)$. The blade-element model is connected to the UBM derived in § 2.1 using the C_T-formulation $f_{Unified}(C_T^{corr}(\mu, \psi), \gamma, \beta)$ (equation (2.17)) to update $a_n(\mu, \psi)$. Here, the momentum model is solved separately at each point over the rotor to account for the azimuthal variation in thrust induced by misalignment (Madsen *et al.* 2020). The tangential induction factor is updated using (Liew *et al.* 2024)

$$a'(\mu, \psi) = \frac{\sigma(\mu) C_{tan}(\mu, \psi) w^2(\mu, \psi)}{4\lambda\mu F(\mu)(1 - a_n)\cos(\gamma) u_\infty^2}. \tag{2.27}$$

After the calculation of the new rotor-normal and tangential induction factors, $a_n(\mu, \psi)$ and $a'(\mu, \psi)$, respectively, we return back to (2.18) to restart the loop. The coupled system is solved using fixed point iteration with relaxation until converged solutions for $a_n(\mu, \phi)$ and $a'(\mu, \psi)$ are reached. Finally, the output rotor-averaged thrust is calculated by integrating over the rotor area

$$\bar{C}_T = \frac{1}{\pi} \int_0^1 \int_0^{2\pi} \mu\sigma(\mu) C_n(\mu, \psi) \frac{w^2(\mu, \psi)}{u_\infty^2} \mathrm{d}\psi \mathrm{d}\mu, \tag{2.28}$$

and similarly the rotor-averaged power coefficient is

$$\bar{C}_P = \frac{1}{\pi} \int_0^1 \int_0^{2\pi} \lambda\mu^2 \sigma(\mu) C_{tan}(\mu, \psi) \frac{w^2(\mu, \psi)}{u_\infty^2} \mathrm{d}\psi \mathrm{d}\mu. \tag{2.29}$$

2.3. *A simple blockage correction based on the UBM*

The Unified BEM method presented in the previous section predicts rotor thrust and power for arbitrary rotor design, tip-speed ratio, pitch angles, rotor-inflow misalignment and blockage ratio. This method solves for the rotor-normal induction using the aerofoil lift and drag coefficients as a thrust closure for the UBM. To compute the rotor power, the aerofoil

https://doi.org/10.1017/jfm.2026.12110 Published online by Cambridge University Press

data are then used to determine the torque contributions along the blades. However, if measurements of rotor thrust and power are available at a single blockage ratio, these can be used to predict C_T and C_P for arbitrary β without the need for a blade-element model, which can be beneficial because the blade-element model requires detailed information on the aerofoils. This methodology is widely referred to as a blockage correction (e.g. Ross & Polagye 2020).

We now use the UBM derived in § 2.1 to develop a simple blockage correction method. While previous work has sought to correct for blockage by identifying a so-called 'equivalent unblocked free-stream velocity' (Ross & Polagye 2020), we instead propose an alternative method that leverages the UBM to directly capture the change in rotor disk velocity induced by blockage. Though in practice these two approaches are similar, the current method provides a new interpretation of the blockage correction in terms of the local rotor performance. This enables an improved understanding of when blockage corrections may be expected to produce reliable predictions. Specifically, it is useful to normalise λ, C_T, and C_P by the rotor-normal disk velocity, $\boldsymbol{u}_d \cdot \hat{n}$, instead of the free-stream velocity u_∞. This yields the local tip-speed ratio λ', local thrust coefficient C_T' and local power coefficient C_P'. Using $\boldsymbol{u}_d \cdot \hat{n} = (1 - a_n)\cos(\gamma)u_\infty$ from (2.1) gives

$$\lambda' = \frac{\lambda}{(1 - a_n)\cos(\gamma)}, \quad C_T' = \frac{C_T}{(1 - a_n)^2 \cos^2(\gamma)}, \quad C_P' = \frac{C_P}{(1 - a_n)^3 \cos^3(\gamma)}. \tag{2.30}$$

This local description of rotor thrust and power in terms of the disk velocity, $C_T'(\lambda')$ and $C_P'(\lambda')$, decouples the rotor performance, which is specific to every turbine, from the induction, in contrast to C_T and C_P where rotor performance and blockage effects are intermingled. As a result, we expect that $C_T'(\lambda')$ and $C_P'(\lambda')$ are independent of β if the aerofoil properties, $C_l(\mu, \alpha)$ and $C_d(\mu, \alpha)$, yaw angle, and pitch angles do not change. A short analysis using the BEM equations is provided in Appendix C to show that C_T' and C_P' depend only on λ', θ_p and γ when $C_l(\mu, \alpha)$ and $C_d(\mu, \alpha)$ are fixed. Blade-resolved simulations are also used to confirm that $C_T'(\lambda')$ and $C_P'(\lambda')$ are constant across a wide range of β in § 4.3. The invariance of C_l and C_d to confinement is a critical assumption for all blockage corrections, and implications of non-constant C_l and C_d, for example due to Reynolds-number effects, are further discussed in § 4.3.

Given the local rotor performance scaling, $C_T'(\lambda')$ and $C_P'(\lambda')$, we now apply it to develop a new blockage correction method. From measurements of $C_T^{\beta_1}$ and $C_P^{\beta_1}$ at an input blockage ratio β_1 and input tip-speed ratio λ^{β_1}, we determine the induction factor $a_n^{\beta_1}$ using the C_T-formulation (equation (2.17)) of the UBM. Using the induction factor at β_1, we compute $C_T'(\lambda')$ and $C_P'(\lambda')$ with (2.30). Next, the C_T'-formulation (2.16) is used to predict the induction factor at an arbitrary output blockage ratio β_2. Finally, the induction at the output blockage ratio is used to determine λ^{β_2}, $C_T^{\beta_2}$ and $C_P^{\beta_2}$ from $C_T'(\lambda')$ and $C_P'(\lambda')$ with (2.30). Therefore, we have a concise and physically justified blockage correction method to map measurements of thrust and power between different blockage ratios for a given rotor of interest. This new blockage correction method based on the UBM is summarised visually in figure 2 and is performed as follows:

(i) Solve the C_T-formulation $f_{Unified}(C_T, \gamma, \beta)$ (equation (2.17)) using the thrust coefficient $C_T^{\beta_1}$ measured at blockage ratio β_1 to determine the induction factor $a_n^{\beta_1}$

$$[a_n^{\beta_1}, \ldots] = f_{Unified}(C_T^{\beta_1}, \gamma, \beta_1). \tag{2.31}$$

https://doi.org/10.1017/jfm.2026.12110 Published online by Cambridge University Press

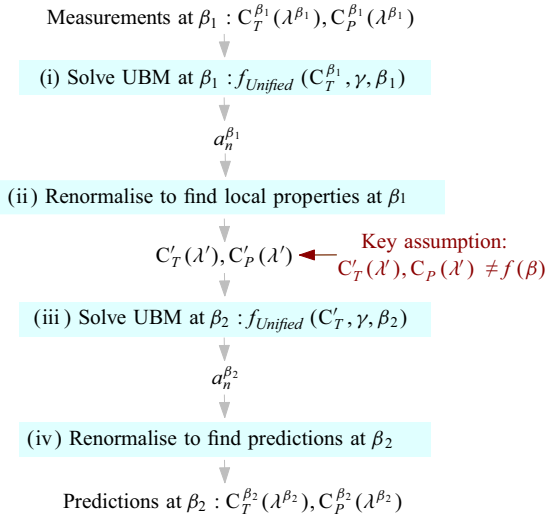


Figure 2. Flow diagram of the blockage correction method presented in § 2.3.

(ii) Use $a_n^{\beta_1}$ to compute the local tip-speed ratio λ', local thrust coefficient C'_T, and local power coefficient C'_P with (2.30) from the data measured at β_1

$$\lambda' = \frac{\lambda^{\beta_1}}{(1 - a_n^{\beta_1})\cos(\gamma)},\ C'_T = \frac{C_T^{\beta_1}}{(1 - a_n^{\beta_1})^2 \cos^2(\gamma)},\ C'_P = \frac{C_P^{\beta_1}}{(1 - a_n^{\beta_1})^3 \cos^3(\gamma)}. \quad (2.32)$$

(iii) Solve the C'_T-formulation $f_{Unified}(C'_T, \gamma, \beta)$ (2.16) to determine the induction factor $a_n^{\beta_2}$ at the blockage ratio β_2

$$[a_n^{\beta_2}, \ldots] = f_{Unified}(C'_T, \gamma, \beta_2). \quad (2.33)$$

(iv) Use $a_n^{\beta_2}$ to determine the output control and performance parameters λ^{β_2}, $C_T^{\beta_2}$ and $C_P^{\beta_2}$ with (2.30)

$$\lambda^{\beta_2} = \lambda'(1 - a_n^{\beta_2})\cos(\gamma), \quad (2.34)$$

$$C_T^{\beta_2} = C'_T(1 - a_n^{\beta_2})^2 \cos^2(\gamma), \quad (2.35)$$

$$C_P^{\beta_2} = C'_P(1 - a_n^{\beta_2})^3 \cos^3(\gamma). \quad (2.36)$$

To summarise, this new blockage correction procedure is a mapping from one combination of blockage ratio, tip-speed ratio, thrust coefficient and power coefficient to another

$$(\beta_1, \lambda^{\beta_1}, C_T^{\beta_1}, C_P^{\beta_1}) \rightarrow (\beta_2, \lambda^{\beta_2}, C_T^{\beta_2}, C_P^{\beta_2}), \quad (2.37)$$

where the mapping is performed by enforcing that C'_T and C'_P are constant for a given λ', pitch angle and rotor-inflow misalignment.

These local parameters C'_T and C'_P can also be interpreted as the unknown rotor performance parameters predicted by the blade-element model. Therefore, measurements at a single β in conjunction with the UBM can be used in place of the blade-element model to make predictions at arbitrary β. This eliminates the need for aerofoil data,

https://doi.org/10.1017/jfm.2026.12110 Published online by Cambridge University Press

Blockage ratio	L_x/D	L_y/D	L_z/D	$N_x \times N_y \times N_z$
$\beta = 0.005$	25	12.5	12.5	$640 \times 800 \times 800$
$\beta = 0.1$	25	2.80	2.80	$640 \times 180 \times 180$
$\beta = 0.2$	25	1.98	1.98	$640 \times 128 \times 128$
$\beta = 0.3$	25	1.62	1.62	$640 \times 128 \times 128$

Table 1. Description of LES domains used for each blockage ratio. The domain lengths and number of grid points in the x, y and z directions are denoted L_x, L_y and L_z, and N_x, N_y and N_z, respectively.

simplifying the modelling effort and reducing uncertainty introduced by the aerofoil polars.

3. Large eddy simulation numerical set-up

We perform LES with PadéOps (Ghate & Lele 2017; Howland *et al.* 2020; Heck & Howland 2025), an open-source, incompressible, pseudo-spectral solver for the filtered Navier–Stokes equations (Subramaniam *et al.* 2021). Relevant details are provided in this section, and the complete numerical description and validation are available in published studies (e.g. Heck & Howland 2025). The sigma subgrid-scale model is used for subgrid-scale stresses (Nicoud *et al.* 2011). The simulations use inflow conditions consistent with the momentum modelling: uniform inflow with zero free-stream turbulence. This inflow is set by a fringe region (Nordström *et al.* 1999) in the x-direction. The turbine is placed $x = 5D$ from the inlet and centred laterally and vertically in the domain. No-flux boundary conditions are used at the rigid sides (y-direction), and periodic boundary conditions are used in the x- and z-directions. The simulation domains used for each blockage ratio are described in table 1. The grid sizes were selected to ensure that the resolution is approximately constant between blockage ratios.

The filtered actuator disk model (ADM) methodology developed by Shapiro *et al.* (2019) is used to model the rotor. The thrust force depends on the local thrust coefficient C_T' and the velocity at the disk $\boldsymbol{u}_d \cdot \hat{n}$ (Calaf *et al.* 2010; Shapiro *et al.* 2019; Heck *et al.* 2023). The actuator disk power is defined as $P = -\boldsymbol{F}_T \cdot \boldsymbol{u}_d$. For the inflow-aligned ($\gamma = 0$) C_T' sweep, a filter width of $\Delta/D = 3.2 \times 10^{-2}$ and a disk thickness of $s = 3\Delta x/2$ are used, following Heck *et al.* (2023). This narrow filter width minimises distortion of the induction, which occurs as a result of smoothing the ADM forcing through filtering. The filtered actuator disk correction factor from Shapiro *et al.* (2019) is turned off since it is not needed because of the narrow filter width used. Additionally, since the correction factor is based on classical momentum theory, which is not valid for the confined case, it would introduce error to the induction of the confined rotor. To simulate misaligned turbines in unconfined flow, Heck *et al.* (2023) rotated the angle of the inflow while keeping the actuator disk aligned with the computational grid. In the present study, simulations of misaligned rotors in a confined channel require the rotor itself to be rotated in order to maintain no-flux boundary conditions at the channel walls. This introduces a trade-off between maintaining a sufficiently narrow filter and ensuring a smooth spatial distribution of the turbine forcing for arbitrary misalignment angles. To balance these requirements, we employ a grid resolution approximately twice as fine in each spatial direction as Heck *et al.* (2023), a filter width of $\Delta/D = 6.5 \times 10^{-2}$ and a disk thickness of $s = 3\Delta x$ for the misaligned cases. Although there is a small sensitivity to the numerical set-up, we find this to be at least an order of magnitude smaller than the effect of blockage. This configuration maintains a relatively narrow filter with minimal influence

https://doi.org/10.1017/jfm.2026.12110 Published online by Cambridge University Press

on induction while ensuring a smoothly distributed forcing for the misaligned ADM. The sensitivity of the simulation results to the numerical set-up of the ADM is presented in Appendix D.

Simulations are run for four flow-through times L_x/u_∞, with the velocity and pressure fields averaged over the final two flow throughs, which is sufficient for convergence of first-order statistics in these zero free-stream turbulence inflow cases (Heck *et al.* 2023). To delineate between the wake and free-stream flow, we compute a streamtube seeded at the rotor disk ($R_s = 0.5D$) in the rotor plane, which may be rotated in the case of yaw misalignment. Wake flow quantities u_4 and $p_{4,w}$ are then extracted by averaging across the yz-plane in a region enclosed by this streamtube at the streamwise location $x = x_0$ (Heck *et al.* 2023; Liew *et al.* 2024). As described in Heck *et al.* (2023), there are some numerical sensitivities in u_4 and $p_{4,w}$ to the rotor representation and to the streamtube seeding but they do not affect the qualitative outcomes of the study. The outlet wake area A_4 is defined as the cross-sectional area of the streamtube at this location. The near-wake length x_0 is defined as the streamwise location at which the minimum yz-averaged streamwise velocity occurred within the streamtube (i.e. the location where turbulent wake recovery begins).

Following Shapiro *et al.* (2018), the spanwise initial wake velocity v_4 is defined as the maximum yz-averaged spanwise velocity within the wake streamtube over $0 \leqslant x/D \leqslant 5$. To estimate the bypass flow quantities, u_s and p_4, a separate streamtube of radius $R_b = 0.55D$ is seeded at the turbine location. The streamwise velocity and pressure are then yz-averaged over the channel cross-section outside this streamtube at $x = x_0$ to obtain u_s and p_4, respectively.

4. Results

This section presents a comparison between the UBM and LES, followed by validation of the Unified BEM and blockage correction methods. The results of the UBM derived in § 2.1, and LES of an actuator disk are presented in § 4.1. In § 4.2, the Unified BEM model developed in § 2.2 is validated against blade-resolved simulations. In § 4.3, the new blockage correction method presented in § 2.3 is validated by mapping rotor thrust and power measurements from blade-resolved simulations, LES of an actuator line model and experimental measurements across a wide range of tip-speed and blockage ratios.

4.1. *Analytical model of an actuator disk in misalignment and blockage*

We begin by comparing the analytical model predictions with LES results for an inflow-aligned actuator disk ($\gamma = 0$), before considering misaligned cases. The induction factor a_n, thrust coefficient C_T and power coefficient C_P from LES and the UBM are shown in figure 3. The analytical model exhibits low error, compared with the LES results, across a wide range of blockage ratios and local thrust coefficients. In particular, the present model accurately represents the rotor dynamics in the limit of low blockage and high thrust, where classical momentum theory is not valid. Predictions from Steiros *et al.* (2022) are included for comparison. The UBM appears to slightly lower error at high local thrust coefficients and blockage ratios compared with the model of Steiros *et al.* (2022) in figure 3, but these relatively minor differences between the predictions for thrust and power coefficients from the models in yaw-aligned conditions are comparable to the numerical uncertainty in the LES (see Appendix D). Figure 3(*a*) shows that the induction factor a_n decreases with increasing blockage ratio β. Consequently, the thrust and power coefficients, which

https://doi.org/10.1017/jfm.2026.12110 Published online by Cambridge University Press

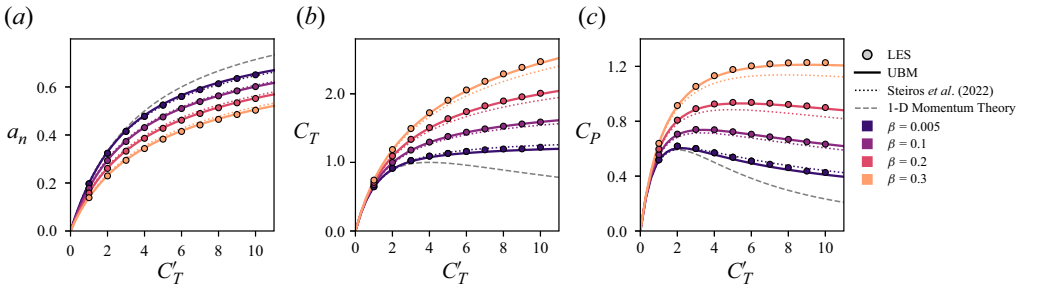


Figure 3. Comparison between the UBM (equations (2.9)–(2.14)) and LES for (*a*) rotor-normal induction, (*b*) thrust coefficient and (*c*) power coefficient across local thrust coefficients C'_T and blockage ratios β with rotor-aligned inflow ($\gamma = 0$). The predictions of classical one-dimensional momentum theory and the blockage model of Steiros *et al.* (2022) are plotted for reference.

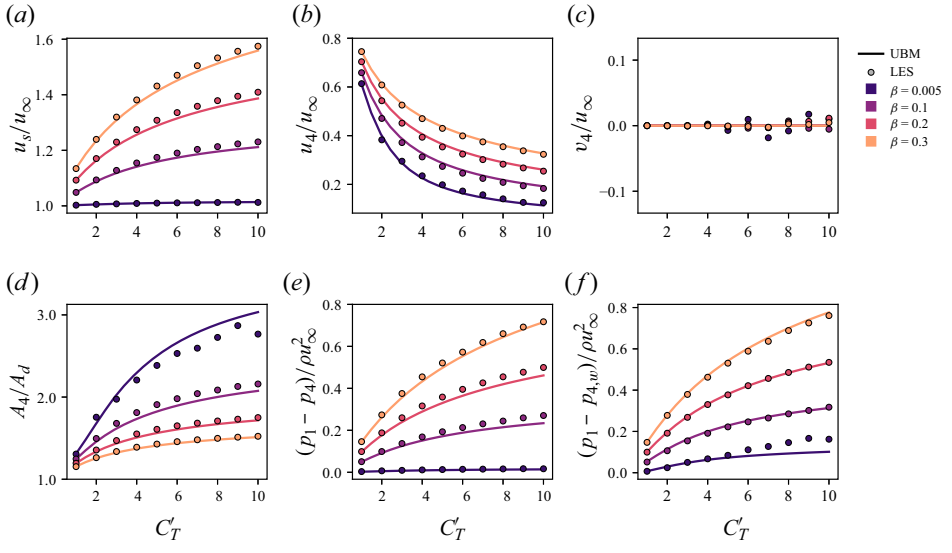


Figure 4. Comparison of (*a*) bypass velocity, (*b*) initial streamwise wake velocity, (*c*) spanwise initial wake velocity, (*d*) outlet wake area, (*e*) bypass pressure drop and (*f*) streamtube pressure drop between the UBM developed in § 2.1 and LES of an actuator disk for various local thrust coefficients C'_T and rotor-aligned inflow ($\gamma = 0$).

scale as $C_T \sim (1 - a_n)^2$ and $C_P \sim (1 - a_n)^3$, respectively, both increase with blockage ratio (figure 3*b*,*c*).

In figure 4, the bypass velocity, streamwise and spanwise wake velocities, outlet wake area and outlet pressures are compared between LES and the UBM. Overall, the model predictions show strong agreement with the LES measurements. Figure 4(*a*) shows that the bypass velocity increases with blockage ratio to satisfy global mass conservation within the channel. Confinement also increases the streamwise wake velocity (figure 4*b*) as the induction factor is reduced. Consequently, the wake expands less, leading to a smaller outlet wake area at higher-blockage ratios (figure 4*d*). Figure 4(*e*) shows that rotor confinement induces a favourable pressure gradient, $p_1 - p_4$, due the acceleration of the bypass flow around the disk. In the absence of blockage, the pressure gradient outside of the streamtube, $p_1 - p_4$, is zero while base suction causes the change in pressure within the streamtube, $p_1 - p_{4,w}$, to be non-zero (figure 4*f*). The model captures the

https://doi.org/10.1017/jfm.2026.12110 Published online by Cambridge University Press

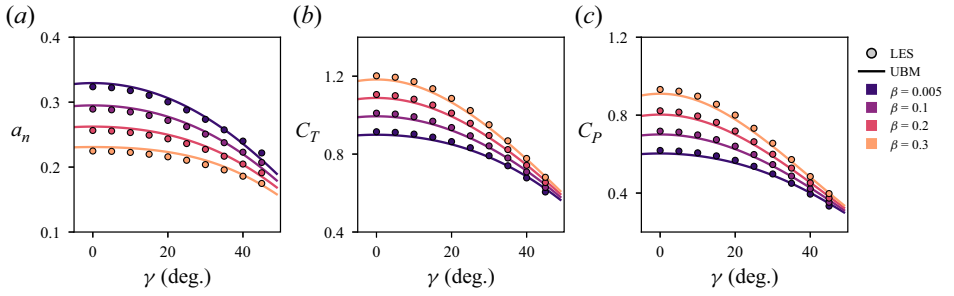


Figure 5. Comparison between the UBM (equations (2.9)–(2.14)) and LES for (*a*) induction factor, (*b*) thrust coefficient and (*c*) power coefficient across misalignment angles γ and blockage ratios β with $C_T' = 2$. Classical momentum theory and the blockage model of Steiros *et al.* (2022) are not shown as they assume perfect alignment between the rotor and inflow.

rotor behaviour in the limit of high thrust and low blockage, where classical momentum theory breaks down, by incorporating the base-suction pressure deficit predicted by the UMM for unconfined flows (Liew *et al.* 2024). As β increases, the pressure gradient increases across the entire channel and dominates the contribution of base suction ($p_1 - p_4 \gg p_4 - p_{4,w}$). Figure 4($f$) demonstrates that the model captures the combined blockage and base-suction pressure contributions across a wide range of β and C_T'.

The blockage-induced favourable pressure gradient, $p_1 - p_4$, allows additional momentum to be extracted from the pressure field. As a result, the disk velocity increases and the induction factor decreases. The blockage-induced pressure gradient increases with rotor thrust, such that blockage effects become more pronounced at higher C_T'. This is consistent with the limit of zero thrust coefficient, where there is no favourable pressure gradient from geometric confinement and therefore no blockage effects. Thus, the blockage effect depends not only on the geometric blockage ratio β but also on its coupling with the thrust coefficient (C_T or C_T').

Having established the rotor-aligned performance, the UBM is next assessed under rotor-misaligned inflow. In figure 5, model predictions of the rotor-normal induction factor a_n, thrust coefficient C_T and power coefficient C_P across misalignment angles γ and blockage ratios β are compared with LES for $C_T' = 2$. For an aligned rotor in unconfined flow, $C_T' = 2$ results in $C_T = 8/9$. Excellent agreement between the LES and the UBM is observed across all misalignment angles and blockage ratios. We note that predictions from the model of Steiros *et al.* (2022) are not shown since that study and model only consider perfect alignment between the turbine and inflow. In figure 5(a), induction decreases with increasing magnitude of misalignment and increasing blockage. As a result of the decreasing induction, the rotor thrust and power coefficients increase with increasing blockage (figure 5b,c). As the misalignment angle increases, both thrust and power decrease, despite the reduction in induction. The quantitative outcome of the reduction in the thrust and power with the misalignment angle will depend on the competition between the geometric reduction in the rotor-normal component of the free-stream flow velocity against the reduction in induction associated with the misalignment. The competition between the geometry and the response of the induction factor is why the thrust and power for a misaligned actuator disk are not accurately modelled by geometry alone (i.e. modelling thrust and power reductions using $\cos^2(\gamma)$ and $\cos^3(\gamma)$, respectively, will lead to errors).

https://doi.org/10.1017/jfm.2026.12110 Published online by Cambridge University Press

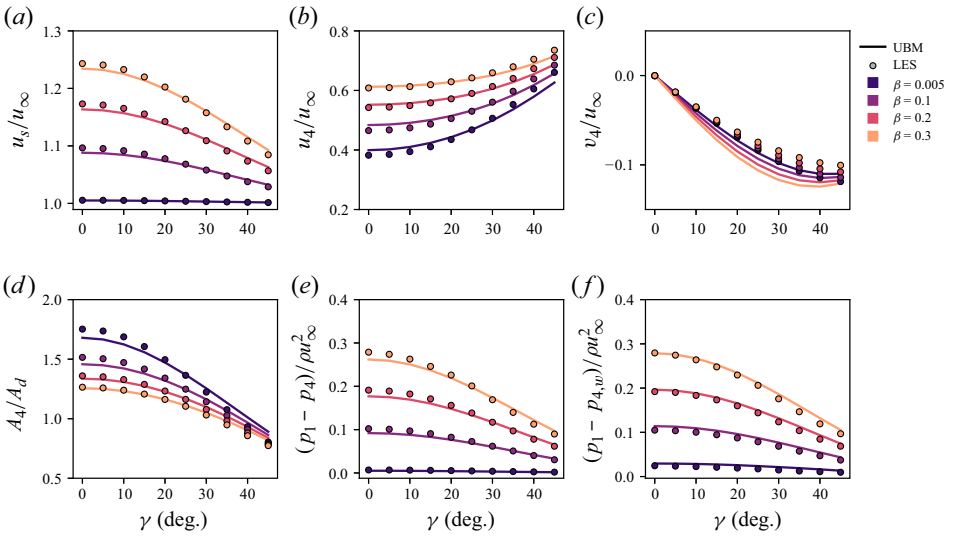


Figure 6. Comparison of (*a*) bypass velocity, (*b*) initial streamwise wake velocity, (*c*) spanwise initial wake velocity, (*d*) outlet wake area, (*e*) bypass pressure drop and (*f*) streamtube pressure drop, between the UBM developed in § 2.1 and LES for various misalignment angles.

In figure 6, the bypass velocity, streamwise and spanwise wake velocities, outlet wake area and outlet pressures from LES and the UBM are shown for the misaligned actuator disk. Overall, the analytical model shows strong agreement with LES. The actuator disk induces a lower bypass velocity as it becomes misaligned with the inflow because both the induction and projected area decrease (figure 6*a*). The reduced induction also causes the streamwise wake velocity to increase with increasing blockage and magnitude of misalignment (figure 6*b*). Figure 6(*c*) shows that the analytical model captures the overall magnitude of the spanwise wake velocity. However, the variations with blockage are reversed relative to the LES predictions. Misalignment reduces induction, causing the wake to expand less, as well as incurring a $\cos(\gamma)$ decrease in the projected area of the rotor, both of which reduce the wake area (figure 6*d*). Figure 6(*e*) demonstrates that the blockage-induced pressure gradient becomes weaker with increasing magnitude of misalignment as a result of the reduced bypass velocity. This reveals that misalignment weakens the blockage effect, as will be discussed further. Finally, figure 6(*f*) shows that the wake pressure measured in LES is also well captured by the model.

In figure 7, we replot the induction, thrust and power of the misaligned rotor normalised by their inflow-aligned ($\gamma = 0$) values for each blockage ratio β. This reveals a central result of the present study: as the blockage ratio increases, the induction factor decreases more gradually with increasing misalignment angle. Correspondingly, as blockage increases, rotor thrust and power decrease more rapidly with increasing misalignment angle. This behaviour arises because rotor misalignment reduces the magnitude of the blockage effect by decreasing both the projected rotor area and the rotor thrust. By lowering the thrust force, misalignment reduces induction. However, the reduced thrust weakens the blockage effect, which would otherwise act to reduce induction as well. As a result, the decrease in induction with misalignment is more gradual when the rotor operates under confinement. The slower reduction in induction implies a lower disk velocity, which leads to a more rapid loss of thrust and power with misalignment when operating in a confined environment. Therefore, the effects of blockage and misalignment are coupled through the turbine thrust force. Due to this coupling, existing models

https://doi.org/10.1017/jfm.2026.12110 Published online by Cambridge University Press

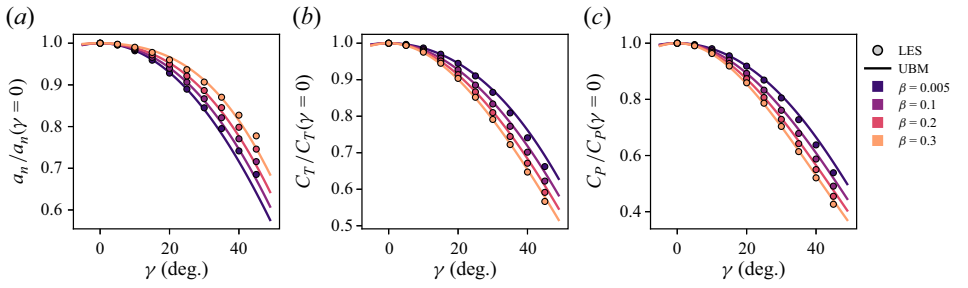


Figure 7. (*a*) Induction factor, (*b*) thrust coefficient and (*c*) power coefficient normalised by their inflow-aligned ($\gamma=0$) values for varying blockage ratios. UBM predictions ((2.9)–(2.14)) and LES results are shown for $C_T'=2$. Increasing blockage leads to a more gradual reduction in induction with misalignment, while thrust and power decrease more rapidly with misalignment.

for misalignment and blockage cannot be superimposed. Instead, these effects must be modelled jointly as provided by the UBM. In addition to implications of these results on measuring thrust and power for misaligned rotors in wind/water tunnels, these results may affect the future design of wake steering flow control for hydrokinetic turbines (Modali *et al.* 2021).

The influence of flow confinement on measured thrust (drag) and power is an important consideration in experimental fluid dynamics. A common approach is to characterise blockage effects using only the geometric blockage (Schottler *et al.* 2018; Upfal *et al.* 2025). However, our results reveal that this is insufficient to characterise the magnitude of blockage effects, owing to its dependence on the thrust coefficient. Consequently, there is no universal blockage ratio below which blockage effects may be considered negligible, as this threshold depends on C_T. We instead propose a more appropriate parameter based on the ratio of the streamwise component of the thrust force, $\boldsymbol{F}_T\cdot\hat{\imath}$, to the free-stream momentum flux scale, $(1/2)\rho A_{CV}u_\infty^2$, yielding $\beta C_T\cos(\gamma)$. Note that in a confined wind/water tunnel setting, this C_T is what would be measured in the experiment, so all information in $\beta C_T\cos(\gamma)$ would be known. To demonstrate this scaling, we quantify the magnitude of blockage effects as the change in thrust and power relative to an unblocked case with the same C_T' and γ, through the thrust ratio $T_r=C_T/C_T(\beta=0)$ and power ratio $P_r=C_P/C_P(\beta=0)$. Figure 8 demonstrates that, unlike β, the proposed parameter captures the leading-order scaling of the blockage-induced increases in thrust and power, quantified by T_r and P_r, respectively. This scaling parameter cannot predict the influence of blockage with the precision of the model developed in § 2.1 but instead provides a simple method for estimating, to first order, the expected augmentation in thrust and power.

We find that this parameter captures the leading-order trend in T_r and P_r across a wide range of practical values of β, C_T and γ (see figure 8). The observed collapse persists beyond the range shown with some sensitivity of the linear fit to the range of β, C_T and γ used. This scaling can be readily evaluated and provides a practical metric for assessing blockage effects in experimental configurations to yield a simple, first-order, quantitative estimate of the approximate change in thrust and power due to blockage effects.

4.2. *Confined blade-element momentum model*

The UBM has been validated against LES of an actuator disk across a wide range of misalignment angles γ, local thrust coefficients C_T' and blockage ratios β in the previous section. However, the UBM is not fully predictive for a rotating turbine, since C_T' depends on the aerofoil characteristics as well as the blade pitch angle θ_p,

https://doi.org/10.1017/jfm.2026.12110 Published online by Cambridge University Press

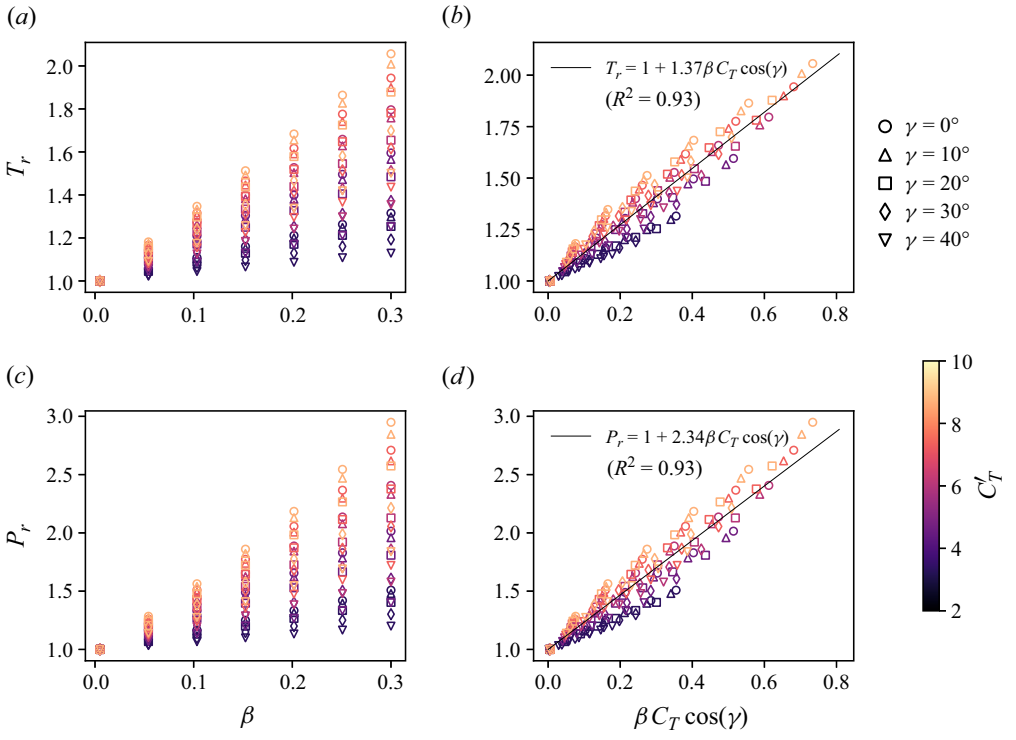


Figure 8. The blockage-induced change in thrust, quantified by T_r, is shown over $0 \leqslant \gamma \leqslant 40°$ and $2 \leqslant C_T' \leqslant 10$ as a function of (*a*) β and (*b*) $\beta C_T \cos(\gamma)$. Panels (*c*, *d*) show the corresponding results for power quantified by P_r.

tip-speed ratio λ and yaw angle γ. Moreover, once a_n is determined, the power of a rotating turbine still explicitly depends on the aerofoil properties and the control setpoints. To address this, we develop a fully predictive Unified BEM model for a rotating turbine under arbitrary blockage and misalignment by coupling the UBM with a blade-element model in § 2.2. Here, we run the Unified BEM model using lift and drag polars of Wimshurst & Willden (2016) for the RISO-A1-24 aerofoil with $Re = 12 \times 10^6$. A three-dimensional stall-delay correction was applied to the lift and drag coefficients of the aerofoil (Du & Selig 1998). MITRotor (Liew *et al.* 2026*a*), an open source tool for physics-based rotor modelling and optimisation, is used to solve the BEM model described in § 2.2. The model is solved using 40 radial grid points.

In figure 9, the Unified BEM predictions are evaluated against the blade-resolved simulations of Wimshurst & Willden (2016). The model reproduces the dependence of thrust and power on tip-speed ratio, and captures the systematic increase in both quantities with blockage. Importantly, the Unified BEM predictions capture the location of peak power across all blockage ratios considered. In general, BEM models rely on blade-element modelling to capture lift and drag forces, using two-dimensional aerofoil polars and empirical submodels for tip losses and three-dimensional stall-delay effects, both of which introduce uncertainty into the model predictions. These uncertainties are distinct from the momentum modelling described in the UBM (the momentum portion of BEM used here), and instead come from the blade-element portion of BEM. These uncertainties are illustrated by the shaded bands plotted in figure 9, encompassing the full spread of

https://doi.org/10.1017/jfm.2026.12110 Published online by Cambridge University Press

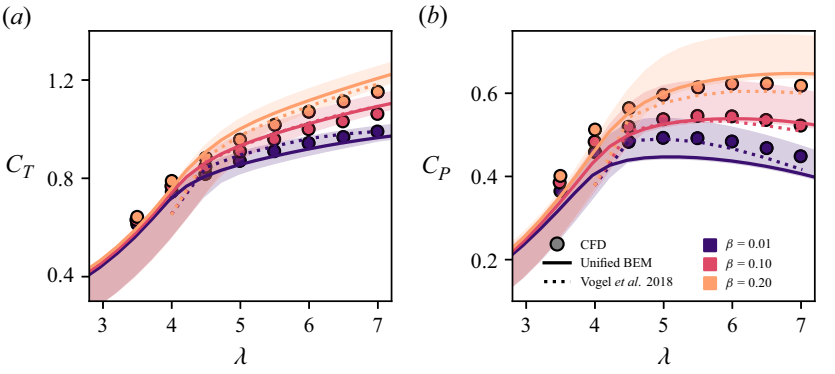


Figure 9. Validation of the Unified BEM method developed in § 2.2 with blade-resolved CFD simulations from Wimshurst & Willden (2016). The earlier BEM model results from Vogel *et al.* (2018) are also shown for comparison. The shaded bands indicate the full spread of results obtained when the radial grid resolution is varied, and the tip loss, three-dimensional stall delay or tangential induction submodels are toggled on or off.

results obtained when the radial grid resolution is reduced to 20 points, and the tip loss, three-dimensional stall delay or tangential induction submodels are toggled on or off.

Quantifying the uncertainty associated with this reasonable range of modelling choices reveals substantial variability in the predictions and highlights the opportunity to improve existing engineering models for the aero/hydrodynamics of rotor blades. Despite these limitations, the overall agreement between the BEM predictions and the blade-resolved simulations is good and comparable to that reported in previous BEM validation studies. Figure 9 further compares the Unified BEM results with the model of Vogel *et al.* (2018), which uses the momentum model developed by Garrett & Cummins (2007). The two BEM models demonstrate similar levels of agreement with the blade-resolved simulations of Wimshurst & Willden (2016). Notably, the Unified BEM method generalises to rotor-inflow misalignment and high thrust coefficient by leveraging the UBM. In the following section, we demonstrate that the errors and uncertainties inherent to blade-element modelling can be eliminated by mapping rotor measurements between blockage ratios using a blockage correction method.

4.3. *Blockage correction method based on the UBM*

In § 4.2, we validated a fully predictive rotor model for arbitrary misalignment angles, thrust coefficients and blockage conditions against blade-resolved simulations. However, the reliance on two-dimensional aerofoil lift and drag polars, together with sub-models for tip losses and three-dimensional aerofoil corrections, introduces errors and uncertainties into BEM-based predictions. Alternatively, if measurements of rotor thrust and power are available at a single blockage ratio, these can be used instead of a blade-element model to make predictions at arbitrary blockage ratios. In § 2.3, we developed a new method that extracts the local thrust coefficient C_T' and local power coefficient C_P' as functions of the local tip-speed ratio λ' using the UBM. This scaling, resulting in blockage-invariant quantities $C_T'(\lambda')$ and $C_P'(\lambda')$, describes the tip speed, thrust and power of the rotor in relation to the rotor-normal disk velocity instead of the free-stream velocity. In Appendix C, we show that when the aerofoil lift and drag curves are independent of blockage, C_T' and C_P' then only depend on λ', θ_p and γ. In this case, we expect such information to be sufficient for predicting the performance of a given rotor at other blockage ratios. In figure 10, we demonstrate the proposed scaling, $C_T'(\lambda')$ and $C_P'(\lambda')$, using the blade-resolved simulations of Wimshurst & Willden (2016). This scaling requires

https://doi.org/10.1017/jfm.2026.12110 Published online by Cambridge University Press

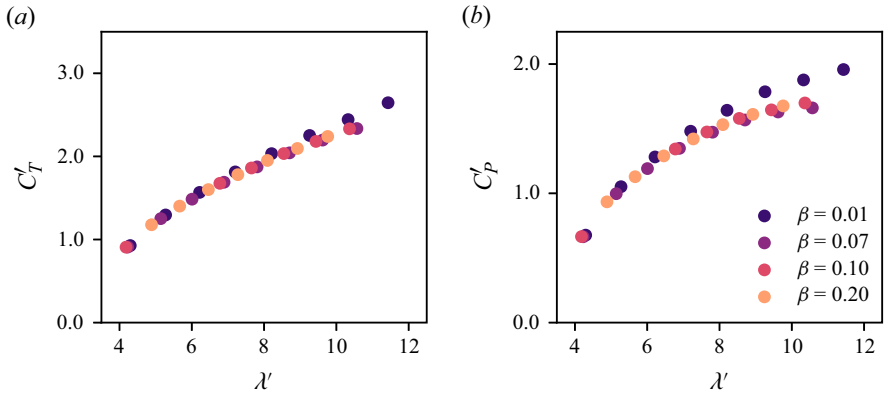


Figure 10. A scaling collapse of the (*a*) thrust and (*b*) power coefficients is demonstrated using the local parameters λ', C'_T and C'_P for blade-resolved simulations from Wimshurst & Willden (2016) over a range of blockage ratios β. The observed collapse supports the validity of the blockage correction method presented in § 2.3.

knowledge of the turbine induction, which is computed using the UBM. In the lowest blockage case ($\beta = 0.01$), C'_T and C'_P are slightly higher than in the blocked cases. Despite this deviation in the unblocked case, the data collapse well overall. The collapse of the data reveals that these local parameters are constant with blockage ratio, supporting the argument presented in Appendix C.

Having verified the proposed scaling, we now apply the blockage correction method developed in § 2.3 to the ADM LES cases shown in § 4.1 and to blade-resolved simulations of Wimshurst & Willden (2016). In figure 11, we apply the blockage correction method outlined in § 2.3 to ADM LES data. In this case, the measurements of the coefficient of thrust (figure 11*a*) and the coefficient of power (figure 11*c*) for the confined flows ($\beta = 0.1,\ 0.2$ and 0.3) are corrected to the unconfined blockage value of $\beta = 0.005$ in figures 11(*b*) and 11(*d*), respectively. Similar to the model comparison with LES presented in § 4.1, the UBM-based blockage correction yields very low error. This very low error is expected, because the core assumption of the blockage correction method proposed in § 2.3 is that the local thrust coefficient C'_T is constant, a feature which is enforced in these LES cases. Nonetheless, these results provide verification that the blockage correction method proposed in § 2.3 yields accuracy consistent with the UBM itself.

We next apply the blockage correction method to a more realistic setting using the blade-resolved simulations of Wimshurst & Willden (2016). In figures 12(*a*) and 12(*b*), the thrust and power coefficients, C_T and C_P, from $\beta = 0.20$ are mapped to $\beta = 0.10$ and $\beta = 0.01$. The blockage-corrected thrust and power coefficients show low error relative to the $\beta = 0.10$ case, reflecting the strong collapse of the blocked cases ($\beta = 0.07,\ 0.10,\ 0.20$) in figure 10. Larger errors occur when mapping to the $\beta = 0.01$ case, consistent with the slight divergence of C'_T and C'_P between blocked and unblocked conditions. This indicates that the remaining error may originate from blockage-induced changes in local rotor performance not accounted for by the correction. In figures 12(*c*) and 12(*d*), we compare the present method with the closed-form corrections of Barnsley & Wellicome (1990) and Steiros *et al.* (2022) to map the $\beta = 0.20$ measurements to $\beta = 0.01$. The present method performs similarly to Steiros *et al.* (2022) while both methods yield notable improvements compared with Barnsley & Wellicome (1990) for higher C_T, achieved at larger values of the tip-speed ratio. Figures 12(*e*) and 12(*f*) shows that the present method and the

https://doi.org/10.1017/jfm.2026.12110 Published online by Cambridge University Press

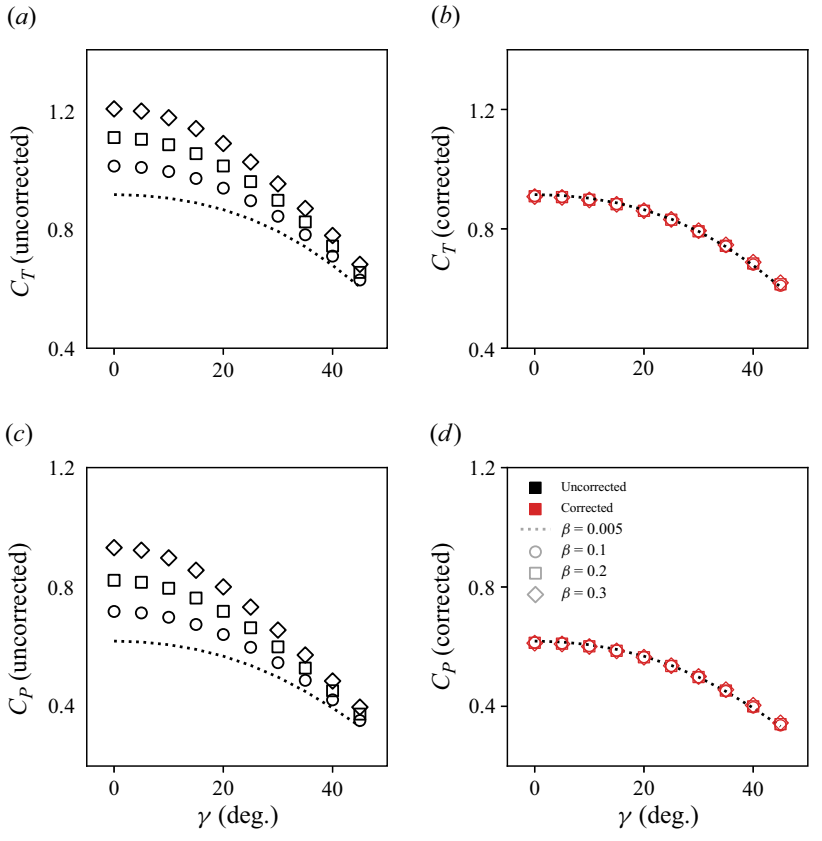


Figure 11. Blockage correction method developed in § 2.3 using the UBM is applied to (*a*) thrust and (*c*) power coefficients from the ADM LES results in (*b*) and (*d*), respectively. The (*c*) thrust and (*d*) power coefficients for low blockage $\beta = 0.005$ are predicted by correcting the thrust and power coefficients from the confined flows ($\beta = 0.1$, 0.2 and 0.3).

correction of Steiros *et al.* (2022) both exhibit excellent agreement when mapping from $\beta = 0.20$ to $\beta = 0.10$. The method of Barnsley & Wellicome (1990) is not shown as it only allows for mapping to $\beta = 0$.

In figure 13, we apply the three corrections to the LES of an actuator line model performed by Steiros *et al.* (2022) for a high solidity (high C_T) rotor. The corrections are used to map the confined ($\beta = 0.20$) thrust and power coefficients to the unconfined ($\beta = 0.03$) results. The three corrections perform similarly at lower tip-speed ratios, but the method of Barnsley & Wellicome (1990) shows significant error at higher tip-speed ratios, corresponding to high thrust coefficients where classical momentum theory is no longer valid. The present model, which accurately captures the dynamics of high-thrust rotors, exhibits lower error across all tip-speed ratios.

Finally, we evaluate the blockage correction methods against experimental data. The experimental dataset of Ross & Polagye (2020) compares the power and thrust of identical axial flow hydrokinetic turbines at two blockage ratios, $\beta = 0.02$ and $\beta = 0.35$. Figure 14 shows the blockage correction developed in § 2.3 as well as the Barnsley & Wellicome (1990) and Steiros *et al.* (2022) methods applied to these measurements. All the corrections show similar discrepancies compared with the low-blockage reference data,

https://doi.org/10.1017/jfm.2026.12110 Published online by Cambridge University Press

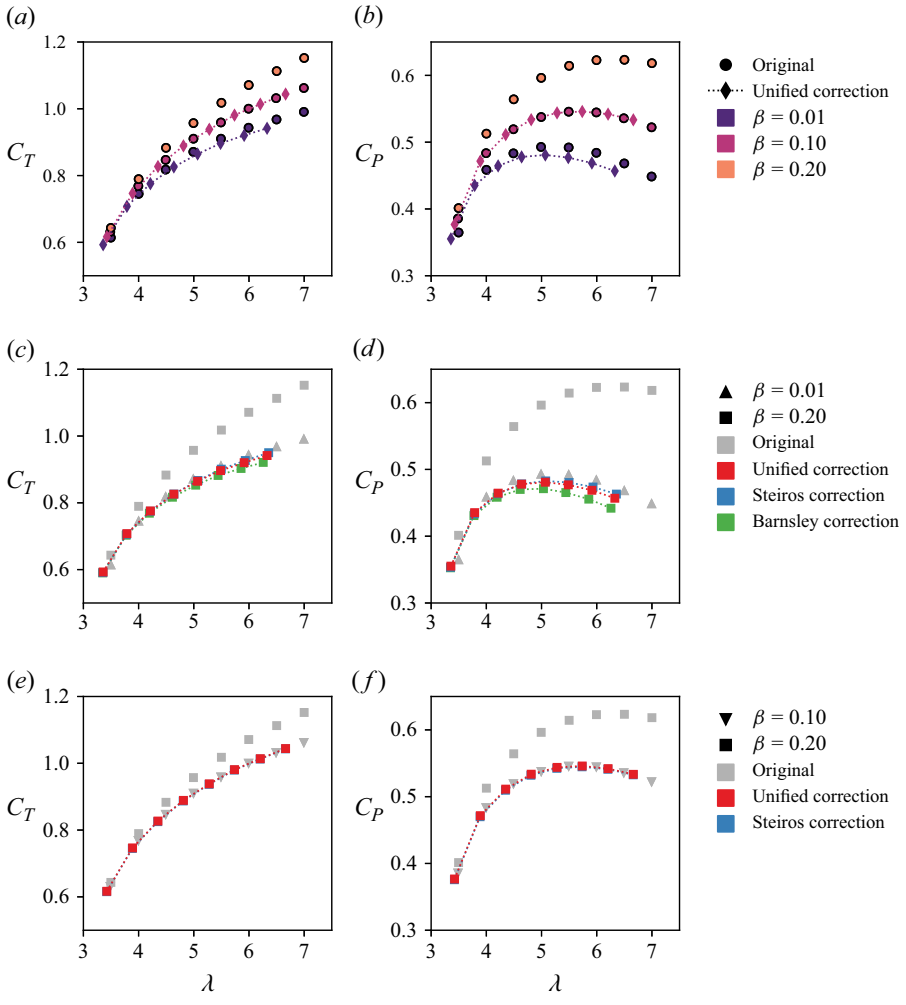


Figure 12. Blockage correction method developed in § 2.3 using the UBM is applied to (*a*) thrust and (*b*) power coefficients from blade-resolved simulations by Wimshurst & Willden (2016). The $\beta = 0.2$ results are mapped to $\beta = 0.1$ and $\beta = 0.01$. (*c*, *d*) The present method is compared with the corrections of Barnsley & Wellicome (1990) and Steiros *et al.* (2022) to map the $\beta = 0.2$ case to $\beta = 0.01$. (*e*, *f*) The present method is compared with the correction of Steiros *et al.* (2022) to map the $\beta = 0.2$ case to $\beta = 0.1$. The correction of Barnsley & Wellicome (1990) is not shown as it only allows for mapping to $\beta = 0$.

particularly for C_P. The lower agreement for C_P is also reported in Ross & Polagye (2020). The relatively large discrepancy in corrected C_P differs notably from the more accurate corrected $C_P(\lambda)$ curves using simulation data shown previously (figures 12 and 13).

To elucidate challenges with blockage corrections in the experimental dataset, we show the scaling to $C_T'(\lambda')$ and $C_P'(\lambda')$ based on the local rotor velocity that underpins the blockage correction model from § 2.3. Figure 15 demonstrates that, unlike the results of Wimshurst & Willden (2016), the Ross & Polagye (2020) dataset does not collapse under the $C_T'(\lambda')$ and $C_P'(\lambda')$ scaling, suggesting that the local rotor performance may be changing with β.

This is acknowledged by Ross & Polagye (2020), who note that blade-level Reynolds-number independence was not maintained across their tests. Specifically, Ross & Polagye

https://doi.org/10.1017/jfm.2026.12110 Published online by Cambridge University Press

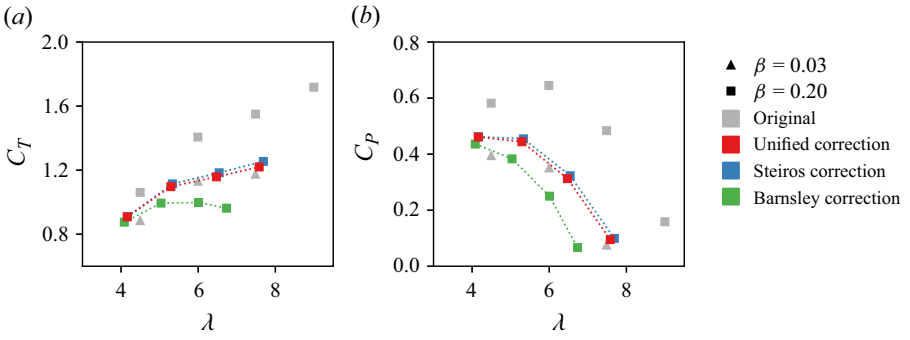


Figure 13. Blockage correction method developed in § 2.3 using the UBM is applied to (*a*) thrust and (*b*) power coefficients from the actuator line simulations of Steiros *et al.* (2022) and compared with the methods of Barnsley & Wellicome (1990) and Steiros *et al.* (2022). The confined ($\beta = 0.20$) case is mapped to the near-unconfined ($\beta = 0.03$) data.

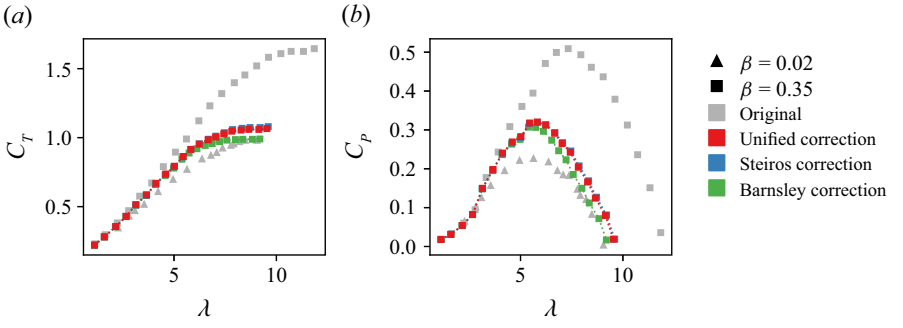


Figure 14. Blockage correction methods applied to the (*a*) thrust and (*b*) power coefficients from the Ross & Polagye (2020) dataset. The confined case ($\beta = 0.35$) case is mapped to the near-unconfined case ($\beta = 0.02$).

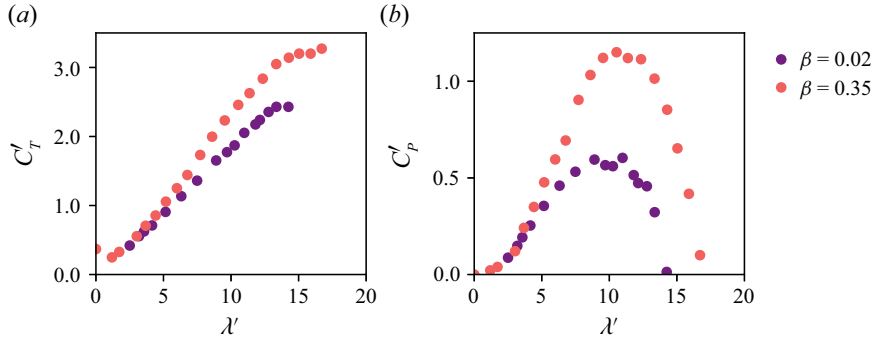


Figure 15. Scaling of the Ross & Polagye (2020) measurements taken at two blockage ratios using the disk velocity computed with the UBM. The results show that (*a*) the local thrust coefficient and (*b*) the local power coefficient do not collapse with λ'.

(2020) noted that rotor performance was sensitive to changes in chord-based Reynolds number. Using their $C_T(\lambda)$ and $C_P(\lambda)$ curves at two chord-based Reynolds numbers, we perform the scaling to $C'_T(\lambda')$ and $C'_P(\lambda')$. As shown in figure 16, these measurements also fail to collapse under the proposed scaling, highlighting that the measurements were

https://doi.org/10.1017/jfm.2026.12110 Published online by Cambridge University Press

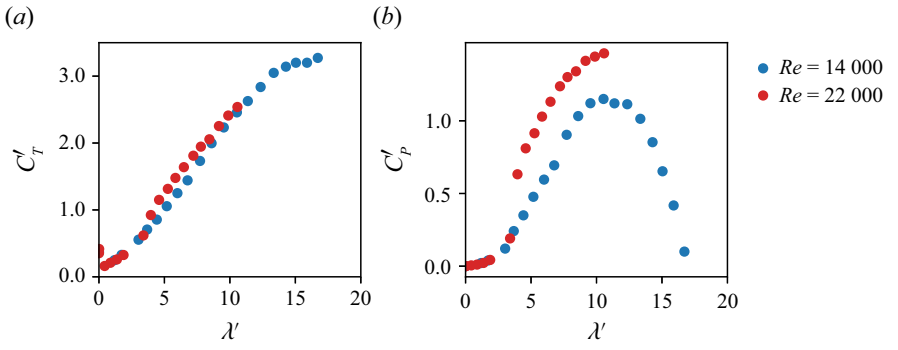


Figure 16. Scaling of the (*a*) thrust and (*b*) power measurements from Ross & Polagye (2020) taken at two Reynolds numbers using the disk velocity computed with the UBM, revealing changes in local rotor performance with Reynolds number.

conducted under conditions where the local rotor performance – and consequently the lift and drag characteristics of the blades – changes with Reynolds number. Since the induction changes with blockage, blockage affects the chord-based Reynolds number, leading to different rotor performances when the blockage is changed.

This Reynolds-number sensitivity violates a key assumption of the blockage correction method, namely that the aerofoil lift and drag curves remain invariant with β. More generally, we expect that any turbine blockage correction approach will fail when trying to correct data that span a significant aero/hydrofoil Reynolds-number dependency unless those dependencies are explicitly and accurately captured in the blockage correction model. This analysis further reveals the need for experimental measurements of identical turbines at multiple blockage ratios and sufficiently high Reynolds number to achieve Reynolds-number independence. Such a dataset would be highly valuable to validate engineering models for rotors operating under blockage.

5. Conclusions

In confined flows, mass conservation requires acceleration of fluid around the rotor, which induces a favourable pressure gradient. This pressure gradient alters the balance of streamwise momentum, increasing the rotor disk velocity relative to unblocked conditions. Consequently, blockage reduces rotor induction while increasing thrust and power. Because the turbine thrust itself generates the blockage-induced pressure gradient, there is a coupled feedback between the thrust force and blockage effects.

Rotor misalignment reduces the rotor-normal disk velocity, lowering the turbine thrust and consequently reducing induction. When a rotor is misaligned in confined flow, misalignment and blockage effects are coupled through the thrust force: misalignment reduces the effective blockage by lowering both the thrust force and the projected rotor area. This mechanism causes the induction factor to decrease more gradually with misalignment in confined flows. As a result, the thrust and power reductions associated with misalignment are exacerbated in confined conditions. Since the misalignment and blockage effects are coupled, they must be modelled jointly as the present approach provides.

This work develops a UBM to predict the induced velocities of an actuator disk across arbitrary blockage ratios, misalignment angles and thrust coefficients. The analytical model is validated against LES, showing excellent agreement with the high-fidelity

https://doi.org/10.1017/jfm.2026.12110 Published online by Cambridge University Press

simulations and lower error than existing models. The model also accurately captures the high-thrust, low-blockage limit by including the base-suction pressure deficit from the UMM for unconfined rotors (Liew *et al.* 2024).

Since the thrust coefficient for an arbitrary rotor design is not known *a priori*, the UBM is not fully predictive for a rotating turbine. Therefore, a Unified BEM model is developed by coupling the validated momentum model with a blade-element closure for the thrust coefficient. This yields a fully predictive rotor model for arbitrary blade design, blockage ratio and control settings. The resulting framework is validated against blade-resolved CFD simulations.

When measurements of rotor thrust and power are available, these can be used to extract the local thrust and power coefficients as functions of the local tip-speed ratio. We identify that if the blade lift and drag properties are independent of blockage, then the local rotor performance is also independent of blockage. This novel scaling is verified with blade-resolved simulation results. We then use this identified scaling to develop a blockage correction method for mapping measurements between arbitrary blockage ratios. The current method provides a new interpretation of the blockage correction in terms of the local rotor performance. This enables an improved understanding of when blockage corrections in general may be expected to produce reliable predictions. The method is validated against blade-resolved simulations, actuator line simulations and experimental measurements of an axial flow turbine. While the blockage correction method yields low errors when correcting simulation data, the blockage correction performs less well for existing experimental data due to the lack of Reynolds-number independence across the different experiments at different blockage ratios. Future work may consider experimental measurements that vary the blockage ratio while ensuring Reynolds-number independence.

The UBM captures the coupled effects of blockage, misalignment and arbitrary thrust coefficient on the induced velocities of an actuator disk. Based on this model, the new blockage correction provides a practical tool to account for blockage effects in turbine and propeller measurements. Finally, the Unified BEM method can be used to optimise the design and control of rotors operating in confined flows, such as hydrokinetic turbines in shallow water or wind turbines in shallow atmospheric boundary layers with stable capping inversions.

Acknowledgements. The authors acknowledge the use of the Stampede3 supercomputer through the NSF ACCESS project, allocation ATM170028, for performing the simulations.

Funding. This work was supported by the National Science Foundation under Grant No. 2542240. K.S.H. was supported by a National Science Foundation Graduate Research Fellowship under Grant No. DGE-2141064.

Declaration of interests. The authors report no conflict of interest.

Appendix A. Base-suction pressure from UMM

The UMM describes the induction of an actuator disk operating in unconfined flow ($\beta \to 0$) for arbitrary thrust coefficient and misalignment angle (Liew *et al.* 2024). The UMM captures the high-thrust regime of rotors by modelling the base-suction effect, which is a persistent pressure drop in the near-wake region. In confined flow, a uniform pressure gradient develops which spans the full channel cross-section and dominates over the contribution of the base-suction pressure deficit. In the present work, we include

https://doi.org/10.1017/jfm.2026.12110 Published online by Cambridge University Press

the base-suction pressure deficit predicted by the UMM to ensure high accuracy across arbitrary blockage levels, misalignment angles and thrust coefficients.

The UMM equations solve for the rotor-normal induction a_n, streamwise wake velocity u_4, lateral wake velocity v_4, near-wake length x_0 and the pressure difference $(p_{4,w} - p_1)$. Note that in the context of UMM, $p_{4,w}$ refers to the pressure within the streamtube at $x = x_0$. The final form of the UMM equations is

$$a_n = 1 - \sqrt{\frac{u_\infty^2 - u_4^2 - v_4^2}{C_T' \cos^2(\gamma) u_\infty^2} - \frac{(p_{4,w} - p_1)}{\frac{1}{2}\rho C_T' \cos^2(\gamma) u_\infty^2}}, \tag{A1}$$

$$u_4 = -\frac{1}{4} C_T' (1 - a_n) \cos^2(\gamma) u_\infty + \frac{u_\infty}{2} + \frac{1}{2}\sqrt{\left(\frac{1}{2} C_T' (1 - a_n) \cos^2(\gamma) u_\infty - u_\infty\right)^2 - \frac{4(p_{4,w} - p_1)}{\rho}}, \tag{A2}$$

$$v_4 = -\frac{1}{4} C_T' (1 - a_n)^2 \sin(\gamma) \cos^2(\gamma) u_\infty, \tag{A3}$$

$$\frac{x_0}{D} = \frac{\cos(\gamma)}{2\beta_s} \frac{u_\infty + u_4}{|u_\infty - u_4|} \sqrt{\frac{(1 - a_n)\cos(\gamma) u_\infty}{u_\infty + u_4}}, \tag{A4}$$

$$p_{4,w} - p_1 = -\frac{1}{2\pi} \rho C_T' (1 - a_n)^2 \cos^2(\gamma) u_\infty^2 \arctan\left[\frac{1}{2}\frac{D}{x_0}\right] + p^{NL}(C_T', \gamma, a_n, x_0), \tag{A5}$$

where the unknown shear layer growth rate parameter is $\beta_s = 0.1403$, based on the analysis of fundamental turbulent jet flow. The near-wake length is predicted by modelling the growth of the shear layers surrounding the wake potential core (Lee & Chu 2003; Bastankhah & Porté-Agel 2016; Liew *et al.* 2024). Despite the presence of these shear layers, turbulent mixing does not significantly influence the dynamics before the near-wake length (Liew *et al.* 2024). Therefore, the inviscid model is sufficient to predict this base-suction pressure term.

The nonlinear pressure field $p^{NL}(x, y)$ as a function of streamwise x and spanwise y directions is computed as

$$p^{NL}(x, y) = \frac{\rho}{2\pi}\left(g_x \circledast \frac{x}{x^2 + y^2} + g_y \circledast \frac{y}{x^2 + y^2}\right), \tag{A6}$$

where $\circledast$ is the two-dimensional convolution operator with advection terms

$$g_x = -\left(w_x \frac{\partial w_x}{\partial x} + w_y \frac{\partial w_x}{\partial y}\right), \tag{A7}$$

$$g_y = -\left(w_x \frac{\partial w_y}{\partial x} + w_y \frac{\partial w_y}{\partial y}\right). \tag{A8}$$

The velocity field is decomposed into background flow and actuator disk-induced component $u = u_\infty + w_x$ and $v = w_y$. There is no free-stream flow v_∞ in the lateral direction. The velocity components are updated using the inviscid Euler equations for the nonlinear induced velocities. This system is solved by iteration and evaluated at

https://doi.org/10.1017/jfm.2026.12110 Published online by Cambridge University Press

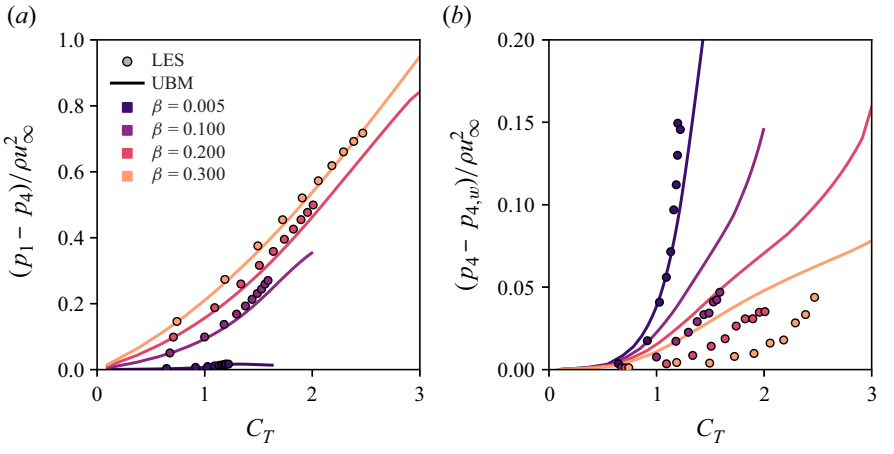


Figure 17. (*a*) Blockage-induced pressure gradient and (*b*) pressure difference between bypass and streamtube flows.

$P^{NL}(x = x_0,\, y = 0)$ which is written as $p^{NL}(C_T', \gamma, a_n, x_0)$. The converged solution to the base-suction pressure in (A5) gives the $p_{UMM}(C_T', \gamma)$ term used to close the UBM.

Appendix B. Model sensitivity to hybrid pressure closure

The hybrid pressure closure presented in § 2.1 combines the blockage-induced pressure gradient with the additional pressure deficit resulting from the base-suction effect of highly loaded rotors. The blockage-induced pressure gradient in the bypass flow $p_1 - p_4$ is plotted in figure 17(*a*) and the difference in pressure between the wake and bypass flows $p_4 - p_{4,w}$ resulting from base-suction effects is plotted in figure 17(*b*). To eliminate sensitivity to the numerical set-up as described in Appendix D, the results are plotted with respect to C_T. The wake pressure deficit $p_4 - p_{4,w}$ is found to decrease as the blockage ratio increases. This is consistent with the limiting case of $\beta \to 1$ where the pressure difference must go to zero. Figure 17 shows that the linear pressure closure $(1 - \beta)p_{UMM}$ of the UBM provides a simple upper bound to the pressure difference and returns to the UMM closure in the unblocked case.

Next, we compare the proposed linear hybrid pressure closure used in § 2.1, $p_{4,w} - p_4 = (1 - \beta)p_{UMM}$, with the two limiting cases in which the full base-suction term from the UMM is included, $p_{4,w} - p_4 = p_{UMM}$, or the base-suction pressure is set to zero, $p_{4,w} - p_4 = 0$. The sensitivity of the model predictions for induction, thrust coefficient and power coefficient to the choice of hybrid pressure closure is shown in figure 18. This test generally demonstrates minimal sensitivity between the different closures. However, omitting the base-suction term entirely introduces significant predictive errors for the very low-blockage cases, as shown in figure 19. This is because in the low-blockage cases, the base-suction pressure term contributes significantly to the dynamics in the absence of a blockage-induced pressure gradient. Conversely, for confined flows, blockage-induced pressure gradients tend to dominate base-suction pressure gradients as shown in figure 17, rendering the interpolation method as a secondary impact for confined flows. Thus, including the hybrid closure is critical because it allows predictions in the low-blockage case (where base suction is a primary pressure effect) and in the higher-blockage cases (where the pressure effect from confinement tends to be more important

https://doi.org/10.1017/jfm.2026.12110 Published online by Cambridge University Press

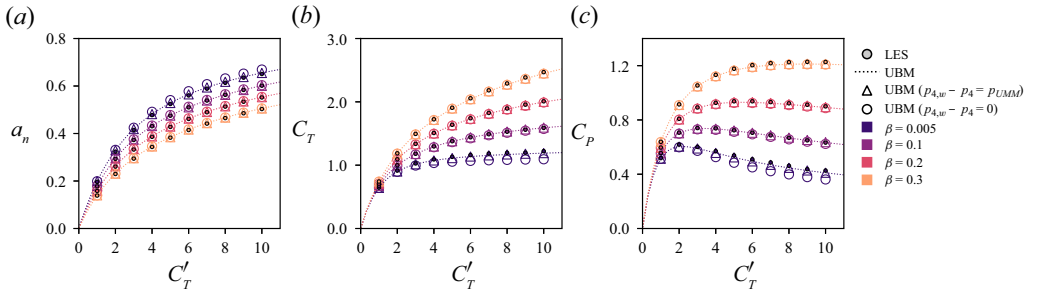


Figure 18. Sensitivity of (a) induction factor, (b) thrust coefficient and (c) power coefficient to pressure closure. The linear interpolation pressure closure, $p_4 - p_{4,w} = (1-\beta)p_{UMM}$, is compared with the two limiting cases: $p_4 - p_{4,w} = p_{UMM}$ and $p_4 - p_{4,w} = 0$.

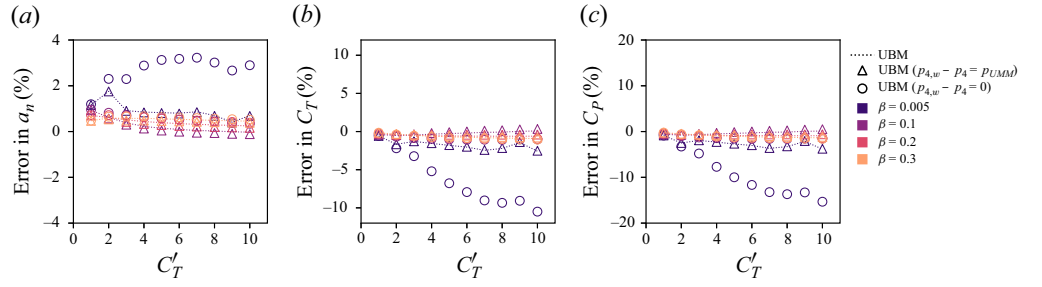


Figure 19. Percent error in (a) induction factor, (b) thrust coefficient and (c) power coefficient relative to LES for each hybrid pressure closure.

than the base-suction pressure), though the specific form of the interpolation has minimal impact.

Appendix C. Local normalisation of blade-element equations

Here, we show that, under a specific set of assumptions, we expect the local thrust and power coefficients C'_T and C'_P to depend only on λ', θ_p and γ, and they are therefore independent of the blockage ratio β. For this analysis, we neglect tangential induction, assume a_n to be constant over the rotor, and assume the aerofoil lift $C_l(\mu, \alpha)$ and drag $C_d(\mu, \alpha)$ are independent of β. These assumptions constrain the inflow velocity at the rotor and the aerofoil performance.

We begin by normalising the axial and tangential relative velocities (equations (2.18) and (2.19)) by the rotor-normal disk velocity $\boldsymbol{u}_d \cdot \hat{n} = (1 - a_n)\cos(\gamma)u_\infty$

$$\frac{v'_n(\mu, \psi)}{u_\infty} = \frac{v_n(\mu, \psi)}{(1-a_n)\cos(\gamma)u_\infty} = 1, \tag{C1}$$

$$\frac{v'_t(\mu, \psi)}{u_\infty} = \frac{v_t(\mu, \psi)}{(1-a_n)\cos(\gamma)u_\infty} = \lambda'\mu - \cos(\psi)\tan(\gamma), \tag{C2}$$

which now depend only on λ' and γ, removing dependence on a_n and therefore also removing dependence on β. Using (2.20) and (2.21) the relative flow speed and angle

https://doi.org/10.1017/jfm.2026.12110 Published online by Cambridge University Press

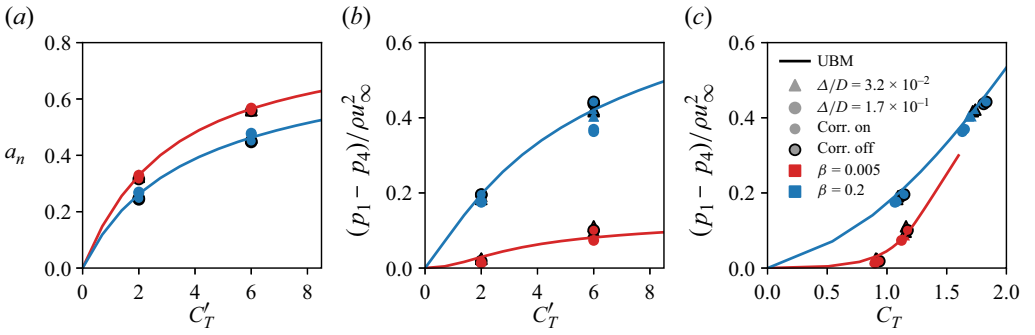


Figure 20. Sensitivity of the LES results to the numerical set-up for (a) induction factor and (b, c) wake pressure deficit. The wake pressure deficit is plotted with respect to the local thrust coefficient in (b), and the resolved thrust coefficient in (c).

become

$$\frac{w'(\mu,\psi)^2}{u_\infty^2} = \frac{w(\mu,\psi)^2}{(1-a_n)^2\cos^2(\gamma)u_\infty^2} = 1 + (\lambda'\mu - \cos(\psi)\tan(\gamma))^2, \tag{C3}$$

$$\phi = \tan^{-1}\left(\frac{1}{\lambda'\mu - \cos(\psi)\tan(\gamma)}\right). \tag{C4}$$

Finally, we can show that C_n and C_{tan} no longer depend on a_n or β. Since $\alpha(\mu,\psi) = \phi(\mu,\psi) - \theta_t(\mu) - \theta_p$ and ϕ is a function of λ' and γ only, then $C_n(\mu,\alpha)$ and $C_{tan}(\mu,\alpha)$ depend only on λ', θ_p and γ.

Using the above expressions, we write the rotor-averaged local thrust coefficient as

$$\overline{C}_T' = \frac{1}{\pi}\int_0^1\int_0^{2\pi} \mu\sigma C_n w'(\mu,\psi)^2 \mathrm{d}\mu\mathrm{d}\psi, \tag{C5}$$

and rotor-averaged local power coefficient as

$$\overline{C}_P' = \frac{1}{\pi}\int_0^1\int_0^{2\pi} \mu^2\lambda'\sigma C_{tan} w'(\mu,\psi)^2 \mathrm{d}\mu\mathrm{d}\psi, \tag{C6}$$

which no longer depend explicitly on a_n and therefore are also independent of β.

This analysis demonstrates that C_T' and C_P' depend only on λ', θ_p and γ, and are independent of both a_n and the blockage ratio β. Consequently, C_T' and C_P' are identical between flows with different blockage ratios when λ', θ_p and γ are matched, enabling the scaling proposed in § 2.3.

Appendix D. Sensitivity of large eddy simulations to numerical set-up

We assess the sensitivity of the LES results to the numerical set-up by conducting simulations while varying the ADM filter width, toggling the Shapiro correction factor on or off (Shapiro *et al.* 2019), and changing the resolution of the simulations. Additional simulations, which are coarsened to the resolution used in Heck *et al.* (2023), are added to compare with the high resolution simulations presented in § 3.

Figure 20(a) shows the spread in rotor-normal induction resulting from varying the numerical set-up of the simulations. All combinations of wide/narrow filter width, ADM correction on/off and high/low resolution are shown with the exception of the high-resolution $\beta = 0.005$ case which was not varied due to computational cost. Similarly,

https://doi.org/10.1017/jfm.2026.12110 Published online by Cambridge University Press

figure 20(*b*) indicates the variation in wake pressure deficit resulting from changing the numerical set-up of the simulations. This sensitivity is due to the direct effect of the numerical set-up on the wake development, as well as the indirect effect of the variation in induction that is triggered by different numerical parameters. In figure 20(*c*), we replot the wake pressure deficit with respect to C_T which eliminates the influence of the change in induction. By plotting the results with respect to the realised thrust force, the results collapse well. This collapse when plotted with respect to the resolved thrust coefficient indicates that the primary sensitivity comes from the change in induction due to the numerical set-up and that the relationship between the thrust coefficient and the induction factor, which is what is modelled in this study, is not sensitive to the numerical set-up. The influence of the ADM set-up on the induction factor has been studied extensively and is well understood (Shapiro *et al.* 2019; Heck *et al.* 2023). In this work, we use a narrow filter width which minimises the influence of the filtering on the induction of the ADM (Heck *et al.* 2023). While the LES results show some quantitative sensitivity to the numerical set-up, this does not change the qualitative conclusions of the study. This numerical sensitivity further motivates future experimental work to measure rotors in confinement and rotor-inflow misalignment across thrust coefficients in the Reynolds-number independent flow regime.

References

Adcock, T.A., Draper, S., Willden, R.H. & Vogel, C.R. 2021 The fluid mechanics of tidal stream energy conversion. *Annu. Rev. Fluid Mech.* **53**, 287–310.

Bahaj, A., Molland, A., Chaplin, J. & Batten, W. 2007 Power and thrust measurements of marine current turbines under various hydrodynamic flow conditions in a cavitation tunnel and a towing tank. *Renew. Energy* **32** (3), 407–426.

Barlow, J.B., Rae, W.H. & Pope, A. 1999 *Low-Speed Wind Tunnel Testing*. John Wiley & Sons.

Barnsley, M. & Wellicome, J. 1990 Final report on the 2nd phase of development and testing of a horizontal axis wind turbine test rig for the investigation of stall regulation aerodynamics. *Tech. Rep.* ETSU.

Bastankhah, M. & Porté-Agel, F. 2016 Experimental and theoretical study of wind turbine wakes in yawed conditions. *J. Fluid Mech.* **806**, 506–541.

Burton, T., Jenkins, N., Sharpe, D. & Bossanyi, E. 2011 *Wind Energy Handbook*. John Wiley & Sons.

Calaf, M., Meneveau, C. & Meyers, J. 2010 Large eddy simulation study of fully developed wind-turbine array boundary layers. *Phys. Fluids* **22** (1), 015110.

Chen, T. & Liou, L. 2011 Blockage corrections in wind tunnel tests of small horizontal-axis wind turbines. *Exp. Therm. Fluid Sci.* **35** (3), 565–569.

Dehtyriov, D. 2023 Flow physics beyond the Betz limit. PhD Thesis, University of Oxford.

Di Mascio, A., Muscari, R. & Dubbioso, G. 2014 On the wake dynamics of a propeller operating in drift. *J. Fluid Mech.* **754**, 263–307.

Du, Z. & Selig, M. 1998 A 3-D stall-delay model for horizontal axis wind turbine performance prediction. In *1998 ASME Wind Energy Symposium*, p. 21. American Institute of Aeronautics and Astronautics (AIAA).

Fleming, P. *et al.* 2019 Initial results from a field campaign of wake steering applied at a commercial wind farm–part 1. *Wind Energy Sci.* **4** (2), 273–285.

Fleming, P., Scholbrock, A., Jehu, A., Davoust, S., Osler, E., Wright, A.D. & Clifton, A. 2014 Field-test results using a nacelle-mounted lidar for improving wind turbine power capture by reducing yaw misalignment. *J. Phys.: Conf. Ser.* **524**, 012002.

Frost, C., Morris, C.E., Mason-Jones, A., O'Doherty, D.M. & O'Doherty, T. 2015 The effect of tidal flow directionality on tidal turbine performance characteristics. *Renew. Energy* **78**, 609–620.

Frost, C.H., Evans, P.S., Harrold, M.J., Mason-Jones, A., O'Doherty, T. & O'Doherty, D.M. 2017 The impact of axial flow misalignment on a tidal turbine. *Renew. Energy* **113**, 1333–1344.

Froude, R.E. 1889 On the part played in propulsion by differences of fluid pressure. *Trans. Inst. Nav. Archit.* **30**, 390.

Froude, W. 1878 On the elementary relation between pitch, slip and propulsive efficiency. *Trans. Inst. Nav. Archit.* **19**, 47.

Garrett, C. & Cummins, P. 2005 The power potential of tidal currents in channels. *Proc. R. Soc. Lond. A: Math. Phys. Engng Sci.* **461** (2060), 2563–2572.

https://doi.org/10.1017/jfm.2026.12110 Published online by Cambridge University Press

GARRETT, C. & CUMMINS, P. 2007 The efficiency of a turbine in a tidal channel. *J. Fluid Mech.* **588**, 243–251.
GHATE, A.S. & LELE, S.K. 2017 Subfilter-scale enrichment of planetary boundary layer large eddy simulation using discrete fourier–gabor modes. *J. Fluid Mech.* **819**, 494–539.
GLAUERT, H. *et al.* 1926 *A General Theory of the Autogyro*, vol. 1111. HM Stationery Office.
GLAUERT, H. 1935 Airplane propellers. In *Aerodynamic Theory*, pp. 169–360. Springer.
HECK, K.S. & HOWLAND, M.F. 2025 Coriolis effects on wind turbine wakes across neutral atmospheric boundary layer regimes. *J. Fluid Mech.* **1008**, A7.
HECK, K.S., JOHLAS, H.M. & HOWLAND, M.F. 2023 Modelling the induction, thrust and power of a yaw-misaligned actuator disk. *J. Fluid Mech.* **959**, A9.
HECK, K.S., MATA, S.A. & HOWLAND, M.F. 2026 Influence of wind shear and veer on power, thrust, and induction of an actuator disk. arXiv: 2606.30830.
HOWLAND, M.F., GHATE, A.S. & LELE, S.K. 2020 Influence of the geostrophic wind direction on the atmospheric boundary layer flow. *J. Fluid Mech.* **883**, A39.
HOWLAND, M.F., QUESADA, J.B., MARTÍNEZ, J.J.P., LARRAÑAGA, F.P., YADAV, N., CHAWLA, J.S., SIVARAM, V. & DABIRI, J.O. 2022 Collective wind farm operation based on a predictive model increases utility-scale energy production. *Nat. Energy* **7** (9), 818–827.
LEE, J.H.-W. & CHU, V.H. 2003 *Turbulent Jets and Plumes: A Lagrangian Approach*, vol. 1. Springer Science & Business Media.
LIEW, J., HECK, K.S. & HOWLAND, M.F. 2024 Unified momentum model for rotor aerodynamics across operating regimes. *Nat. Commun.* **15** (1), 6658.
LIEW, J., UPFAL, I.M.L., GERING, S.A., HECK, K.S. & HOWLAND, M. 2026*a* Howland-Lab/MITRotor (Version 0.2.3) [Computer software]. Zenodo. https://doi.org/10.5281/zenodo.21938405
LIEW, J., UPFAL, I.M.L., GERING, S.A., HECK, K.S. & HOWLAND, M. 2026*b* Howland-Lab/Unified-Momentum-Model (Version v0.5.0) [Computer software]. Zenodo. https://doi.org/10.5281/zenodo.20644355
MADSEN, H.A., LARSEN, T.J., PIRRUNG, G.R., LI, A. & ZAHLE, F. 2020 Implementation of the blade element momentum model on a polar grid and its aeroelastic load impact. *Wind Energy Sci.* **5** (1), 1–27.
MEYERS, J., BOTTASSO, C., DYKES, K., FLEMING, P., GEBRAAD, P., GIEBEL, G., GÖÇMEN, T. & VAN WINGERDEN, J.-W. 2022 Wind farm flow control: prospects and challenges. *Wind Energy Sci.* **7** (6), 2271–2306.
MIKKELSEN, R. & SØRENSEN, J. 2002 Modeling of wind tunnel blockage. In *Proceedings of the 2002 Global Windpower Conference and Exhibit*. European Wind Energy Association.
MODALI, P.K., VINOD, A. & BANERJEE, A. 2021 Towards a better understanding of yawed turbine wake for efficient wake steering in tidal arrays. *Renew. Energy* **177**, 482–494.
NDINDAYINO, O., PUEL, A. & MEYERS, J. 2025 Effect of blockage on wind turbine power and wake development. *Wind Energy Sci.* **10** (9), 2079–2098.
NICOUD, F., TODA, H.B., CABRIT, O., BOSE, S. & LEE, J. 2011 Using singular values to build a subgrid-scale model for large eddy simulations. *Phys. Fluids* **23** (8), 085106.
NISHINO, T. & WILLDEN, R.H. 2012 Effects of 3-D channel blockage and turbulent wake mixing on the limit of power extraction by tidal turbines. *Intl J. Heat Fluid Flow* **37**, 123–135.
NISHINO, T. & WILLDEN, R.H. 2013 The efficiency of tidal fences: a brief review and further discussion on the effect of wake mixing. In *International Conference on Offshore Mechanics and Arctic Engineering*, vol. 55423, p. V008T09A010. American Society of Mechanical Engineers.
NORDSTRÖM, J., NORDIN, N. & HENNINGSON, D. 1999 The fringe region technique and the Fourier method used in the direct numerical simulation of spatially evolving viscous flows. *SIAM J. Sci. Comput.* **20** (4), 1365–1393.
PIANO, M., NEILL, S., LEWIS, M., ROBINS, P., HASHEMI, M.R., DAVIES, A., WARD, S. & ROBERTS, M. 2017 Tidal stream resource assessment uncertainty due to flow asymmetry and turbine yaw misalignment. *Renew. Energy* **114**, 1363–1375.
RANKINE, W.J. 1865 On the mechanical principals of the action of propellers. *Trans. Inst. Nav. Archit.* **6**, 13.
ROSHKO, A. 1955 On the wake and drag of bluff bodies. *J. Aeronaut. Sci.* **22** (2), 124–132.
ROSS, H. & POLAGYE, B. 2020 An experimental assessment of analytical blockage corrections for turbines. *Renew. Energy* **152**, 1328–1341.
SCHOTTLER, J., BARTL, J., MÜHLE, F., SÆTRAN, L., PEINKE, J. & HÖLLING, M. 2018 Wind tunnel experiments on wind turbine wakes in yaw: redefining the wake width. *Wind Energy Sci.* **3** (1), 257–273.
SEGALINI, A. & INGHELS, P. 2014 Confinement effects in wind-turbine and propeller measurements. *J. Fluid Mech.* **756**, 110–129.

https://doi.org/10.1017/jfm.2026.12110 Published online by Cambridge University Press

SHAPIRO, C.R., GAYME, D.F. & MENEVEAU, C. 2018 Modelling yawed wind turbine wakes: a lifting line approach. *J. Fluid Mech.* **841**, R1.
SHAPIRO, C.R., GAYME, D.F. & MENEVEAU, C. 2019 Filtered actuator disks: theory and application to wind turbine models in large eddy simulation. *Wind Energy* **22** (10), 1414–1420.
SØRENSEN, J.N. 2011 Aerodynamic aspects of wind energy conversion. *Annu. Rev. Fluid Mech.* **43**, 427–448.
SØRENSEN, J.N. 2016 *General Momentum Theory for Horizontal Axis Wind Turbines*, vol. 4. Springer.
STEIROS, K., BEMPEDELIS, N. & CICOLIN, M.M. 2022 An analytical blockage correction model for high-solidity turbines. *J. Fluid Mech.* **948**, A57.
STEIROS, K. & HULTMARK, M. 2018 Drag on flat plates of arbitrary porosity. *J. Fluid Mech.* **853**, R3.
SUBRAMANIAM, A., GHATE, A., GHAISAS, N.S. & HOWLAND, M.F. 2021 PadeOps GitHub repository. GitHub [Computer software]. Available at: https://github.com/Howland-lab/PadeOps. (last accessed August 5, 2021).
TAMARO, S., CAMPAGNOLO, F. & BOTTASSO, C.L. 2024 On the power and control of a misaligned rotor–beyond the cosine law. *Wind Energy Sci.* **9** (7), 1547–1575.
UPFAL, I.M.L., ZHU, Y., HANDY-CARDENAS, E. & BREUER, K. 2025 Shape-morphing membranes augment the performance of oscillating foil energy harvesting turbines. *Phys. Rev. Fluids* **10**, 034702.
VAN KUIK, G.A. 2007 The Lanchester–Betz–Joukowsky limit. *Wind Energy: Intl J. Prog. Applics Wind Power Convers. Technol.* **10** (3), 289–291.
VOGEL, C., WILLDEN, R. & HOULSBY, G. 2018 Blade element momentum theory for a tidal turbine. *Ocean Engng* **169**, 215–226.
WERLE, M. 2010 Wind turbine wall-blockage performance corrections. *J. Propul. Power* **26** (6), 1317–1321.
WIMSHURST, A. & WILLDEN, R. 2016 Computational analysis of blockage designed tidal turbine rotors. In *Progress in Renewable Energies Offshore*, pp. 587–600. CRC Press.

https://doi.org/10.1017/jfm.2026.12110 Published online by Cambridge University Press